

1

2 Sager, W.W., Bull, J.M. and Krishna, K.S. (2013) Active faulting on
3 the Ninetyeast Ridge and its relation to deformation of the Indo-
4 Australian plate. *Journal of Geophysical Research: Solid Earth*, 118,
5 (8), 4648-4668.([doi:10.1002/jgrb.50319](https://doi.org/10.1002/jgrb.50319)).

6

7 **Active Faulting on the Ninetyeast Ridge and its Relation to Deformation**
8 **of the Indo-Australian Plate**

9 W. W. Sager^{1,2}, J. M. Bull³, and K. S. Krishna⁴

10 ¹Department of Oceanography, Texas A&M University, College Station, TX, 77843
11 USA, wsager@tamu.edu

12 ²[Now at Department of Earth and Atmospheric Sciences, University of Houston,](#)
13 [Houston, TX 77240, \[wwsager@uh.edu\]\(mailto:wwsager@uh.edu\)](#)

14 ³School of Ocean and Earth Science, National Oceanography Centre Southampton,
15 University of Southampton, Southampton SO14 3ZH, UK , bull@noc.soton.ac.uk

16 ⁴CSIR - National Institute of Oceanography, Dona Paula, Goa 403004, India,
17 krishna@nio.org

18 **Abstract**

19 The ~4500 km-long Ninetyeast Ridge (NER) in the northeastern Indian Ocean
20 crosses a broad zone of deformation where the Indo-Australian plate is fracturing into
21 three smaller plates (India, Capricorn, Australia) separated by diffuse boundaries whose
22 extents are poorly defined. New multichannel seismic reflection profiles image active
23 faults along the entire length of the NER and show spatial changes in the style of
24 deformation along the ridge. The northern NER (0-5°N) displays transpressional motion
25 along WNW-ESE faults. Observed fault patterns confirm strike-slip motion at the
26 western extent of the April 2012 Wharton Basin earthquake swarm. In the central NER
27 (5-8°S), deformation on WNW-ESE-trending thrust faults implies nearly N-S
28 compression. An abrupt change in fault style occurs between 8° and 11°S, with modest,
29 extension characterizing the southern NER (11-27°S). Although extension is dominant,
30 narrow zones of faults with strike-slip or compressional character also occur in the
31 southern NER, suggesting a complex combination of fault motions. At all sites, active
32 faulting is controlled by the reactivation of original, spreading-center formed, normal
33 faults, implying that deformation is opportunistic and focused along existing zones of
34 weakness, even when original fault trend is oblique to the direction of relative plate
35 motion. Observed faulting can be interpreted as India-Australia deformation in the
36 northern NER and Capricorn-Australia deformation in the southern NER. The India-
37 Capricorn boundary is directly adjacent to the northern NER and this juxtaposition
38 combined with a different style of faulting to the east of the NER imply that the ridge is a
39 tectonic boundary.

40 **1. Introduction**

41 The vast Indo-Australian plate in the central Indian Ocean is breaking into three
42 smaller pieces separated by diffuse boundaries (Fig. 1) [*Royer and Gordon, 1997*].
43 Although this location is perhaps the best-documented distributed deformation within an
44 oceanic plate [*Gordon, 2000*], many details are lacking owing to the large extent and
45 remote location of the affected area. Compressional faults and folds occur in the Central
46 Indian Basin south of India and west of the Ninetyeast Ridge (NER) [*Weissel et al., 1980*;
47 *Petroy and Wiens, 1989*; *Bull and Scrutton, 1992*; *Krishna et al., 2001*; *Delescluse and*
48 *Chamot Rooke, 2007*]. In contrast, deformation is mainly by strike-slip faulting in the
49 Wharton Basin to the east of the NER [*Petroy and Wiens, 1989*; *Stein et al., 1989*; *Deplus*
50 *et al., 1998*; *Deplus, 2001*]. In the middle of this deformed zone, the NER is a long
51 (~4500 km) volcanic ridge that displays active seismicity in some locations, but the
52 nature of deformation is unclear because geophysical data are sparse in the region. If the
53 NER is only a passive weal on the oceanic lithosphere, it may simply respond to broad-
54 scale tectonic forces with little change to the pattern of faulting extending from adjacent
55 basins. Alternatively, it has been suggested that the NER is a mechanical boundary owing
56 to the apparent change in deformation across it [*e.g., Delescluse and Chamot-Rooke,*
57 *2007*], so faulting may be complex. We examined new multichannel seismic reflection
58 profiles and multibeam bathymetry data from the NER to understand its role in the
59 fracturing of the Indo-Australian plate. We find evidence of active faulting of variable
60 style along its entire length. In this report, we document this faulting and explore
61 implications for the location and style of diffuse plate boundaries.

62 **1.1 Tectonic Development of the Indo-Australian Plate and Formation of the NER**

63 The Indo-Australian plate is a Cenozoic amalgamation of two pre-existing plates,
64 India and Australia. During the rifting of Gondwana, both plates formed on the north
65 side of spreading ridges that separated the northward-drifting continents from Antarctica
66 [Norton and Sclater, 1979]. Because both plates drifted almost exactly northward
67 relative to Antarctica and have not rotated significantly, the Indo-Australian plate
68 contains many fracture zones trending approximately N-S with nearly E-W trending
69 magnetic anomalies in between. India and Australia continued as separate plates until the
70 time of anomaly 19 (~42 Ma [Cande and Kent, 1995]) when the Wharton Ridge (located
71 east of the NER, separating India and Australia) jumped southward to form the
72 continuous Southeast Indian Ridge [Royer et al., 1991; Krishna et al., 1995]. At that
73 time, the India and Australia plates were combined.

74 The NER trends nearly N-S and stretches from 31°S at Broken Ridge to 10°N,
75 where it disappears beneath sediments of the Bengal Fan (Fig. 1). Magnetic lineation
76 breaks and satellite altimetry data show that the NER is nearly parallel to fracture zones
77 formed at a paleo-spreading ridge that once separated the India and Australia plates
78 [Royer and Sandwell, 1989; Krishna et al., 1995; 2012]. Many different authors have
79 explained the formation of the NER as a result of various tectonic anomalies [see review
80 by Royer et al., 1991], but the modern consensus is that it was created by hotspot
81 volcanism that emplaced a ridge on the northward drifting Indian plate from Late
82 Cretaceous to early Cenozoic time [Royer et al., 1991; Krishna et al., 2012]. The hotspot
83 was often located near the spreading ridge [Sager et al., 2010; Krishna et al., 2012] and
84 changes in NER morphology may be related to the proximity of the hotspot to the

85 spreading ridge [Royer *et al.*, 1991]. Because of its near-ridge location, the hotspot
86 emplaced material on both the Indian and Antarctic plates, with most of the volcanic
87 product ending up on the India plate owing to repeated southward ridge jumps [Krishna
88 *et al.*, 2012]. Nevertheless, the hotspot volcanism produced a remarkably linear age
89 progression that ranges from 77 Ma at Ocean Drilling Program (ODP) Site 758, in the
90 northern NER, to 43 Ma at Deep Sea Drilling Project (DSDP) Site 254 in the southern
91 NER [Krishna *et al.*, 2012]. At ~42 Ma, the large-scale reorganization of spreading
92 centers that brought together the India and Australia plates also moved the hotspot
93 permanently beneath the Antarctic plate, ceasing the NER formation [Royer *et al.*, 1991;
94 Krishna *et al.*, 2012].

95 **1.2 Diffuse Plate Boundaries in the Central Indian Ocean**

96 Plate geometry, seafloor spreading data, and differences in crustal gravity lineations
97 indicate that the northern NER is the location of a diffuse triple junction [Royer and
98 Gordon, 1997] (Fig. 1). Because this triple junction implies that three wide plate
99 boundaries come together, each with different stress fields, different styles of
100 deformation are expected along the NER as it traverses these boundary zones.

101 Euler poles describing relative plate motions occur within two of the diffuse
102 boundaries and as a result, the style of deformation changes along each of these
103 boundaries from extension to compression [Gordon, 2000]. The India-Capricorn Euler
104 pole is located near the equator, close to the Chagos-Laccadive Ridge (Fig. 1) [Royer and
105 Gordon, 1997; DeMets *et al.*, 2010], implying compression south of India and extension
106 between the Chagos-Laccadive Ridge and the Carlsberg Ridge. The Capricorn-Australia
107 pole is located at the southern end of the NER [Royer and Gordon, 1997; DeMets *et al.*,

108 2010], implying a zone of extension from the Southeast Indian Ridge (SEIR) to the
109 southern NER and compression farther north. In contrast, only compression is expected
110 along the India-Australia boundary, located southwest of the Java Trench, because the
111 Euler pole describing that plate pair is situated in the Central Indian Basin, ~1000 km
112 away from that boundary [Royer and Gordon, 1997; DeMets et al., 2010; Bull et al.,
113 2010].

114 South of India, distributed deformation occurs within the India-Capricorn plate
115 boundary and is characterized by E-W thrust faults spaced 5-10 km apart and long
116 wavelength (100-300 km) folds [Weissel et al., 1980; Wiens et al., 1986; Bull and
117 Scrutton, 1992]. The thrust faults result from nearly N-S compression reactivating nearly
118 E-W normal faults that were formed in the ocean crust by seafloor spreading [Bull and
119 Scrutton, 1992]. This deformation extends across a broad zone to the west side of the
120 NER (Fig. 1) and began 14-18 Myr ago [Krishna et al., 2009; Bull et al., 2010].

121 Earthquakes and seismic reflection profiles in the Wharton Basin imply that it is
122 broken into narrow slivers by reactivation of the nearly N-S trending fracture zones by
123 left-lateral strike-slip motion [Delescluse and Chamot Rooke, 2007; Deplus et al., 1998;
124 Deplus, 2001]. The lateral extent of this reactivation is unclear but has been observed in
125 geophysical data near the equator [Deplus et al., 1998] and in the form of strike-slip
126 earthquakes along fracture zones in the wedge between the Java Trench and the NER
127 [Delescluse and Chamot Rooke, 2007; Satriano et al., 2012]. Although a few NE-SW
128 trending gravity lineations are observed in this region perpendicular to the convergent
129 plate motion direction [Petroy and Wiens, 1989; Stein et al., 1990], the trend of
130 reactivated fracture zones is oblique to the direction of compressive stress and

131 presumably this mismatch between stress and fault direction is a result of opportunistic
132 fracturing along inherited zones of weakness caused by original crustal faults.

133 Few earthquakes occur along the southern NER and faulting is poorly documented in
134 this region, so deformation on the Capricorn-Australia boundary is unclear and the
135 boundary may be as much as 2000 km in width [DeMets *et al.*, 2010]. The nature of this
136 boundary in the vicinity of the NER south of the equator is simply not known.

137 **1.3 Seismicity in the Vicinity of the NER**

138 Earthquakes occur in a diffuse zone across the Central Indian Basin and Wharton
139 Basin from $\sim 35^\circ\text{S}$ to $\sim 7^\circ\text{N}$ (Fig. 2) [e.g., Delescluse and Chamot Rooke, 2007]. The
140 greatest seismic activity occurs in a band stretching NE-SW from the Java Trench, across
141 the northern NER, into the Central Indian Basin south of India. Near the Java Trench,
142 events are mainly NE thrust faults related to subduction. In the Central Indian Basin, near
143 the equator, these events also display dominantly thrust focal mechanisms, but oriented
144 N-S with some strike-slip mechanisms mixed in (Fig. 2). This pattern is thought to result
145 from compression between the India and Capricorn plates, with thrusting taking place
146 where original normal faults in the oceanic crust are reactivated and strike-slip events
147 occurring on N-S-trending fracture zones [Petroy and Wiens, 1989; Bull and Scrutton,
148 1990; Delescluse *et al.*, 2008].

149 South of $\sim 5^\circ\text{S}$, earthquakes define a sparse NE-SW oriented band that includes the
150 NER. As a result, earthquakes in the Wharton Basin are observed to the north of $\sim 17^\circ\text{S}$
151 whereas those in the Central Indian Basin are mainly south of $\sim 18^\circ\text{S}$ (Fig. 2). Strike-slip
152 focal mechanisms with WNW-ESE/ENE-WSW nodal planes dominate in the northern
153 Wharton Basin [Petroy and Wiens, 1989; Royer and Gordon, 1997]. They occur mostly

154 in the wedge-shaped area from the northern NER to the Java Trench and south to $\sim 15^{\circ}\text{S}$
155 and are thought to result mainly from Late Cretaceous and early Cenozoic fracture zones
156 that have been reactivated as left-lateral strike-slip faults [*Deplus et al., 1998; Deplus,*
157 *2001; Delescluse et al., 2012*]. Some of these earthquakes have been remarkably strong
158 for oceanic earthquakes [e.g., *Robinson et al., 2001*], including a Mw 7.9 shock in 2000
159 and two recent tremors, Mw 8.6 and 8.2, that occurred on 11 April 2012 [*Satriano et al.,*
160 *2012; McGuire and Beroza, 2012; Meng et al., 2012*]. South of $\sim 10^{\circ}\text{S}$, focal
161 mechanisms indicate mostly strike-slip and thrust faults, with the former having similar
162 nodal planes to strike-slip mechanisms farther north and the latter showing NW-SE
163 convergence (Fig. 2). At about 10°S , a few thrust focal mechanisms are observed in the
164 Wharton Basin (Fig. 2) near a low SW-NE trending ridge that parallels gravity lineations.
165 These mechanisms may indicate thrust faulting along that feature. A small number of
166 extensional focal mechanisms occur to the southwest of the NER (mostly farther south
167 than the extent of Figure 2), caused by divergence south of the Capricorn-Australia Euler
168 pole [*Royer and Gordon, 1987*].

169 Northern NER earthquakes display similar strike-slip mechanisms to nearby
170 Wharton Basin earthquakes and because the nearly N-S nodal plane is close to the trend
171 of the NER, it was proposed that ENE-WSW strike-slip faults occur along the NER
172 [*Stein and Okal, 1978*]. The seismic energy radiation pattern and aftershock distribution
173 of the 2012 Wharton Basin events indicate that faulting in the northern Wharton Basin
174 and NER is more complex [*Satriano et al., 2012; McGuire and Beroza, 2012; Delescluse*
175 *et al., 2012; Meng et al., 2012*]. Although the two main shocks of this cluster align with
176 the expected trend of original Wharton Basin fracture zones, it appears that the

177 earthquake swarm activated a lattice of WNW-ESE right lateral strike-slip faults [*Meng*
178 *et al.*, 2012]. The aftershocks included the northern NER and imply nearly E-W strike-
179 slip faults in that area [*Meng et al.*, 2012].

180 **1.4 Faulting on the NER**

181 Given the diffuse deformation and seismicity in the area, faulting is expected on the
182 NER. Most published observations of NER faults are isolated examples that do not give
183 a comprehensive picture [*Veevers, 1974; Naini and Eittreim, 1974; Curray and*
184 *Munashinge, 1989; Shipboard Scientific Party, 1989a, 1989b*]. Virtually all faults
185 reported in prior publications appear to be normal, except for one profile that apparently
186 shows thrust faults on the east side of the southern NER near DSDP Site 214 [*Pilipenko,*
187 *1996*]. E-W trending normal faults have been reported along the length of the NER
188 [*Pilipenko, 1996; Sager et al., 2010*]. They often form rotated fault blocks and grabens
189 and were probably formed by tension near the spreading ridge during NER formation
190 [*Sager et al., 2010*].

191 **2. Data and Methods**

192 High-resolution multibeam bathymetry data and 10-fold multichannel seismic
193 (MCS) profiles were collected over the NER during cruise KNOX06RR of the R/V
194 *Roger Revelle* [*Sager et al., 2007*]. Multibeam data were acquired using a 12 kHz
195 Kongsberg Simrad EM120 sonar system, which yielded swaths of data 10-30 km in
196 width, allowing detailed imaging of the seafloor at the survey sites.

197 More than 3700 km of MCS data were collected at six sites, four of which are
198 coincident with ODP or DSDP drill sites (Sites 214, 216, 253, and 758). The seismic
199 system used a 48-channel hydrophone array (streamer) and the source consisted of two

200 generator-injector (GI) airguns with generator volumes of 45 in³ (737 cm³) and injector
201 volumes of 105 in³ (1720 cm³). Seismic data were processed to CDP stack and time
202 migration was produced assuming a single velocity of 1500 ms⁻¹.

203 “Acoustic basement” was recognized as a strong (high acoustic impedance
204 contrast), widespread reflector beneath which seismic returns were absent, incoherent, or
205 reflectors were intermittent. Throughout much of the study area, acoustic basement was a
206 sharp, well-defined horizon. At a few locations, acoustic basement was absent or
207 extended in depth (i.e., a thick package of reflections) with an appearance similar to
208 sediments in places, perhaps indicating the seismic waves did not reach the igneous pile.
209 In most cases the acoustic basement horizon likely represents the top of the igneous rock
210 beneath the sedimentary section. However, in places where the horizon is thick or has
211 sedimentary characteristics, basement may be volcanoclastic sediments, such as the thick
212 section of volcanic ash cored at DSDP Site 253 [*Shipboard Scientific Party, 1974*].

213 Faults were recognized by vertical offsets or discontinuities of sedimentary layers,
214 monoclinical folds, bowing or kinking of sedimentary layers, coherent diffractions cutting
215 sediment horizons, narrow troughs with sediment fill, and narrow grabens. Some faults
216 show extensive deformation over an extended area and are probably the result of fault
217 zones with a number of smaller faults that cannot be recognized individually. Active
218 faults were recognized by the fact that they extend through the sedimentary section from
219 basement to the surface, either causing a seafloor offset or disturbance of recent
220 sediments.

221 Because of the wide spacing of survey sites, we searched for older seismic data
222 that show faults in the NER. Somewhat useful data were collected on three cruises of the

223 R/V *Robert Conrad* during 1986 that surveyed ODP drill sites (cruises RC2705, RC2707,
224 and RC2708). A single channel streamer was used as the receiver and a single 80 in³
225 (1320 cm³) water gun was used as a source [Newman and Sclater, 1988]. Analog seismic
226 profiles from these cruises were obtained from Lamont Doherty Earth Observatory. In
227 addition, a small amount of similar single-channel seismic data collected during ODP
228 Leg 121 was also examined at Site 757 [Shipboard Scientific Party, 1989a; 1989b].

229 **3. NER Fault Observations**

230 Faults were interpreted by observing diagnostic features in seismic sections as
231 described in the previous section and are shown in figures by symbols on bathymetry
232 maps and in seismic sections by arrows that indicate the locations of fault traces near the
233 seafloor. In this section we describe the types of motion inferred from the observed
234 faults. Owing to inadequate imaging or ambiguous geometry, it was not possible to
235 interpret the motions of all faults (usually shown by gray arrows in the figures).

236 **3.1 Site 758 (5.2°N)**

237 Site 758 multibeam bathymetry data cover the southern end of a large seamount
238 and two small seamounts to its south (Fig. 3). These data clearly image the fractured
239 nature of the seafloor in the vicinity of the two small seamounts. Approximately 10
240 bathymetric lineations striking WNW-ESE (~N100°E) are observed crossing almost the
241 entire multibeam data set (Fig. 3). These lineations appear to be small ridges and/or
242 escarpments, often with paired troughs. Bathymetric contours have a “jagged”
243 appearance, with sharp, nearly right angle offsets of 3-10 km in many places (Fig. 3).
244 These displacements give the appearance that the bathymetric features have been offset.

245 Notably, the two small seamounts have nearly N-S trending flank contours that appear to
246 have been offset by ~10 km along the lineation in between them.

247 Seismic data show that the NER near Site 758 is extensively faulted (Fig. 4).
248 Faults are apparent on N-S trending seismic lines but are rarely noted on E-W oriented
249 seismic lines, implying that the faults trend nearly E-W, as do the bathymetric lineations.
250 The bathymetric lineations correspond to major faults that show significant offset at the
251 seafloor (e.g., faults 1-2, 6-7, 8; numbers in Fig. 4).

252 Observed faulting at Site 758 implies both compression and strike-slip motion.
253 Compression is indicated by the upwarp of layers (between faults 1-2 and 4-5) and up-
254 thrust acoustic basement (“pop-up”) features such as the small block between faults 6-7
255 and the asymmetric ridge at fault 8. Compression also explains the geometry of fault 3,
256 which shows a break in sediment layers that are upturned at the fault.

257 Strike-slip motion is implied by faults that separate sedimentary sections of
258 different thickness and different seismic character, as observed across faults 1-2. In
259 addition, this fault pair is likely a flower structure because the faults appear to converge
260 at depth. Strike-slip motion is also implied by the observed offsets in bathymetric
261 contours.

262 Two of the active Site 758 faults connect with offsets of acoustic basement (faults
263 2, 8). It is difficult to determine whether active faulting is the cause of the offsets
264 because the overlying sediment cover is too thin to compare the sedimentary and
265 basement offsets.

266 Cruise RC2705 seismic data cover a broader area than the KNOX06RR survey
267 and show that faulting is widespread, being observed on all seismic lines (Fig. 5). Where
268 the RC2705 data overlap the multibeam bathymetry, bathymetric lineations correlate with
269 faults (Fig. 4). The resolution of these older data is mediocre and it is difficult to discern
270 details of the faults below the seafloor. Most are recognized only by notches or offsets of
271 the seafloor; although, fault 1 (Fig. 6) displays an asymmetric basement block uplift like
272 that of fault 8 in Figure 4.

273 **3.2 Site 216 (1.5°N)**

274 Multibeam bathymetry data at Site 216 (Fig. 7) show lineations with WNW-ESE
275 trends (~N100°E to N110°E) stretching across the top and east flank of a large seamount.
276 These lineations are mostly troughs incising the sediments. In addition, contours on the
277 eastern flank of the seamount appear jagged, with right angle (mostly left lateral) offsets
278 of a few kilometers, often occurring where intersected by the bathymetric lineations.
279 Seismic sections show that the bathymetric lineations correspond to larger, active faults
280 (faults 2, 3, 5-6, 8; numbers in Fig. 8). Faults are seen most clearly on N-S oriented lines
281 but also are detected on lines with other orientations, consistent with the orientation of
282 the nearly E-W bathymetry lineations.

283 Site 216 faulting has similar characteristics to that of Site 758, indicating both
284 compression and strike-slip motion. Compression is indicated by fault 7, which has
285 reversed geometry and occurs at the south edge of a basement pop-up block. Other
286 evidence for compression is the upwarp of sediment layers and acoustic basement
287 observed north of fault 3, between faults 5-6, 9-10, and at fault 8. Fault 3 displays a
288 sharp kink in sediment layering, which may have the same cause.

289 The highly-deformed sag trough of fault 2 is a structure commonly observed on
290 strike slip faults. In addition, the sediment layers across this fault have different
291 thicknesses, indicating lateral motion. Sedimentary layers also change thickness and
292 character across faults 4, 7, 8, and 10, likewise implying lateral movements. In the case
293 of fault 8, this observation implies that both reverse and strike-slip motion occurred.
294 Strike-slip faulting is also consistent with the observation of laterally-offset bathymetry
295 contours.

296 Offsets of acoustic basement are observed for faults 1, 6, and 7. For the latter
297 two, the acoustic basement offset is larger than the sediment offset, indicating that an
298 older basement fault was reactivated. For fault 1, the offset of acoustic basement and
299 sediment layers is approximately the same, implying that faulting at later stage caused the
300 acoustic basement to develop an offset.

301 **3.3 Site NER2 (6.7°S)**

302 Site NER2 encompasses most of a flat-topped seamount with shallow valleys
303 across its top, a steep western flank, and a shallow eastern flank that extends eastward out
304 of the survey (Fig. 9). E-W bathymetric lineations also occur at this site; however, they
305 are not as distinct as at Sites 216 and 758. The most prominent lineation is the trough at
306 the south flank of the seamount, which is a large graben that was probably formed during
307 the construction of the NER [Sager *et al.*, 2010]. Other lineations have similar trends
308 crossing the top of the seamount, with several being traced across the entire summit (Fig.
309 9). Some seamount bathymetry contours have an angular nature, rather than being
310 rounded, and in several places have right angle bends and offsets similar to those seen at

311 sites 758 and 216. These offsets show no consistent trend, some being right-lateral and
312 others left-lateral.

313 Seismic lines show that the NER2 seamount is extensively faulted and the
314 bathymetric lineations are correlated with major faults (Figs. 9, 10). Compression is
315 clearly indicated by fault 4, which has a reversed geometry with the hanging wall
316 upthrust and bending of sedimentary layers (Fig. 10). Fault 3 is similar, but the reverse
317 geometry is not as clear. Other evidence of compression is the upwarp of sediment layers
318 observed between faults 1-2, 2-3, 8-9 and near fault 10. Faults 8-9 are associated with a
319 basement pop-up structure. Warping on the north side of fault 11 may also indicate
320 compression. This fault may also have a component of strike-slip motion as indicated by
321 the deformed trough and by slight differences in sediment character across the fault.
322 Fault 6 appears as a small, negative (extensional) flower structure, with two closely
323 spaced faults converging at depth. This fault may indicate strike-slip motion with a small
324 extensional component.

325 A number of active faults are rooted in offsets of acoustic basement (faults 4, 5, 7,
326 8, 9). For most of these, the basement offset is greater than that within the sediments or
327 at the surface, implying reactivation of a pre-existing basement fault.

328 **3.4 Site NER3 (7.7°S)**

329 Site NER3 covers much of a small, N-S-trending ridge segment (Fig. 11).
330 Although not as prominent as at other locations, bathymetric lineations are also observed
331 on the summit of the NER3 seamount. Most have nearly E-W trends, but there is
332 significant variability. These lineations correlate with active faults and summit basin

333 edges, implying that active deformation affects the seafloor topography. Unlike other
334 sites farther north, there are no apparent offset contours. NER3 acoustic basement is
335 highly dissected and offset, mostly from early extensional faults that formed rotated fault
336 blocks, probably formed during construction [*Sager et al., 2010*]. These faults strike
337 approximately E-W (Fig. 11) and appear to account for much of the broader topography
338 and the bathymetric lineations, which are formed by fault troughs or ridges.

339 Fault geometries imply that both compression and strike-slip faulting occur at this
340 site, with the former being dominant. Compression is indicated by reverse faults 14 and
341 15 (numbers in Fig. 12). Both faults show hanging walls upthrust relative to footwalls.
342 Fault 3 also appears to be reverse, with basement on the south side upthrust (Fig. 12).
343 Upwarped sediments indicate compression and are observed at faults 4, 10, 11, 14, 16,
344 and perhaps between 5-6 and 8-9. The folds at faults 11 and 14 are large enough to
345 create ridges imaged by the multibeam bathymetry. Compression is also indicated by the
346 basement pop-up feature at fault 14.

347 Strike-slip motion is suggested by subtle differences in sedimentary layer
348 thicknesses across a few faults. This situation occurs at faults 5, 6, 11, perhaps at 14, and
349 across faults 2-3 and 7-8 (Fig. 12). Faults 2-3 form a sag trough similar to features often
350 observed on strike-slip faults. Because fault 3 is a reverse fault, the combination of
351 interpreted compressive and strike-slip motions implies transpression across this set of
352 faults. Faults 7-8 form a graben that is reminiscent of the fault 2-3 trough. Although the
353 sense of motion is not obvious, the upwarp of sediment layers on the south side of this
354 pair likely indicates compression.

355 Seismic profiles show extensive early deformation of the NER3 ridge in the form
356 of offset and tilted fault blocks that appear normal in nature (Fig. 12B). Many of the
357 active faults connect to these basement offsets. In most cases, the offset of acoustic
358 basement is greater than that of overlying sediments (faults 1, 6, 10, 12-13, 15), implying
359 recent reactivation of an original basement fault. For fault 8, the offset of acoustic
360 basement is similar to that of upper sediment layers, suggesting that the entire basement
361 offset resulted from the active faulting. For fault 14, surface expression appears greater
362 than basement offset because of an expanded recent sediment section caused by recent
363 differential sedimentation.

364 **3.5 Site 214 (11.3°S)**

365 The Site 214 survey encompasses a broad area at the northern end of the high,
366 continuous ridge that makes up the southern NER. The surveyed portion of the ridge
367 summit contains three uplifts separated by two swales, both trending ~N70°E (Fig. 13),
368 that apparently formed from extension during formation of the NER [Sager *et al.*, 2010].
369 Bathymetric lineations are few and no offset bathymetric contours are evident (Fig. 13).

370 Seismic sections in the Site 214 area show extensive faulting and most faults
371 appear to be normal faults as indicated by the hanging wall having moved downward
372 relative to the footwall (e.g., faults 7-11, 12-13, 17, 21, 22; numbers in Fig. 14).
373 Although the stress regime appears dominantly tensional, indications of possible
374 compression and strike-slip are observed. Sediment layer upwarp is noted between faults
375 2-3 and 4-6, implying compression. Sediment layers at faults 1 and 3 have a v-shape that
376 may indicate strike-slip motion. Thus, it appears that a regime of slight extension is
377 punctuated by zones of compression and strike-slip motion.

378 Acoustic basement is highly dissected at Site 214, with sediment infill indicating
379 that this intense normal faulting occurred at the time of or soon after ridge construction
380 [Sager *et al.*, 2010]. Many of the active faults are rooted in these original faults. In
381 almost every case an increase in displacement with depth is consistent with basement
382 fault reactivation.

383 **3.6 Site 757 (17.1°S)**

384 Multibeam bathymetry data around Site 757 were collected by R/V *Sonne* [Flueh
385 and Reichert, 1998; Grevemeyer *et al.*, 2001] and single channel seismic data come from
386 cruises RC2707 and ODP Leg 121. The bathymetry map (Fig. 15) shows that the site is
387 located atop the broad dome of a large seamount and there are few bathymetric contours
388 or features of interest. Small (<100 ms TWTT) offsets in the seafloor were mapped
389 (Figs. 15, 16) and are similar to those produced elsewhere by active faulting. Most faults
390 (e.g., numbers 1-3 in Fig. 16) appear to have normal fault geometry, with fallen footwalls
391 creating steep escarpments. Data quality is mediocre, with little detail imaged below the
392 seafloor, so fault interpretation is less certain than sites with recent data.

393 **3.7 Site 253 (25.5°S)**

394 The Site 253 survey is slightly offset from the DSDP drill site (Fig. 17) and
395 covers an area of the southern NER that is dissected by a large, NE-trending canyon.
396 Satellite-predicted bathymetry data [Smith and Sandwell, 1997] imply that the ridge is
397 rugged, with number of local highs and lows on the ridge top. Only a few tectonic
398 lineations are noted in the multibeam bathymetry data (Fig. 17), trending NE-SW
399 (~N70°E to N80°E).

400 Seismic data show that this part of the ridge also experienced extensive early
401 faulting during or shortly after construction, creating large offsets in the acoustic
402 basement as well as large grabens, most of which are filled by sediments (Fig. 18).
403 Seismic sections also show widespread active faulting. Most faults have small offsets
404 (<50 ms TWTT), but a few are larger, especially at the edges of large offset basement
405 fault blocks. Some cause small offsets and undulations of the seafloor (faults 1-9, 13, 17;
406 numbers in Fig. 18) and others are connected with small (fault 12) or large troughs (faults
407 14-15, 16, 18-20, 21, 22-23). Overall, the faults at Site 253 are mostly normal faults, but
408 there are some indications of other types of motion. Although inter-fault sediment
409 reflectors between faults 1-9 appear to be folded, an observation that could signify
410 compression, we interpret this geometry simply as coeval deformation and sedimentation
411 between closely-spaced normal faults within a zone of intense faulting (at mid-sediment
412 layer depths the faults are clearly normal and layer bending is insignificant). Fault 1
413 occurs at the edge of a small basement uplift that may have resulted from recent
414 compression because the sediment layer offset is approximately the same as the acoustic
415 basement offset.

416 Most active faults are connected to offsets in acoustic basement. For many, the
417 offset of basement or deep sediment layers is approximately the same as that in the upper
418 sediments, implying that the basement offset is a result of the recent faulting (faults 1, 5-
419 8, 13). Fault 17 shows less offset at seafloor than basement offset, whereas faults 21-23
420 have more seafloor topography than offset in deep layers. The former observation
421 implies that an original basement fault was reactivated whereas the latter observation
422 suggests that erosion may be a factor in creating these troughs. In some locations, the

423 sense of faulting may have changed. Faults 15 and 19 appear to be connected with
424 basement reverse faults, but the seafloor troughs (bounded by faults 14-15, 18-20)
425 indicate extension. These observations imply the reactivation of original basement faults
426 but with a different motion of the active faulting.

427 **3.8 Site 756 (27.3°S)**

428 No multibeam bathymetry data are available from Site 756. Satellite-predicted
429 bathymetry data [*Smith and Sandwell, 1997*] imply that the surface of the NER at this site
430 has significant topography (Figs. 15, 16) similar to nearby Site 253. Single-channel
431 seismic data from R/V *Robert Conrad* cruise RC2708 show numerous seafloor offsets
432 that are consistent with active faulting (Fig. 16). Although the geometries of most are
433 unclear, faults 4 and 5 (numbers in Fig. 16) appear to have normal geometry. Faults are
434 observed on most seismic lines, both N-S and E-W trending, implying that the fault
435 trends are SW-NE, similar to the bathymetric trends and fault trends at Site 253. Data
436 from Site 756 are of such low quality that little detail is seen below the seafloor, making
437 unique interpretations of fault nature difficult. Active faulting is indicated, but the sense
438 of most faults is uncertain.

439 **4. Discussion**

440 High-resolution multibeam bathymetry data and 2D multichannel seismic data
441 clearly show active faulting along the entire length of the NER. Although our data have
442 higher resolution than previous NER data sets, both the wide spacing of sites and the
443 coarse spacing of seismic lines at each survey site are limitations to the resolution of the
444 study. Within the survey sites, seismic lines are widely spaced, hampering definition of
445 fault geometry. Many faults have small offsets, are inadequately imaged, or have

446 ambiguous geometry, all of which also make some fault interpretations ambiguous.
447 Despite these cautions, the data are far better than any previously available and allow us
448 to make important observations about NER faulting.

449 **4.1 Reactivation of Original NER Faults**

450 Active faults visible at the seabed are usually connected with near-vertical steps in
451 the top of acoustic basement (the top of the NER volcanic pile). Analysis of differences
452 in the vertical separation of sediment layers relative to the throw on basement faults
453 indicates whether the recent faulting caused the basement fault or whether a pre-existing
454 fault was reactivated. In some instances the vertical offsets of the sedimentary and
455 basement faults are the same, implying that recent deformation caused the basement
456 offset. For many active faults the basement offset is greater than sediment offset,
457 implying that recent faulting reactivated an original basement fault. The reactivation of
458 pre-existing weaknesses by diffuse plate boundary faulting of the Indo-Australian plate is
459 not a new observation. The same occurs in the Central Indian Basin, where original
460 spreading-ridge-generated normal faults are reactivated as active thrust faults [*Bull and*
461 *Scrutton, 1992*]. Similarly, strike-slip faulting in the Wharton Basin is thought to occur
462 by the reactivation of original transform faults [*Deplus, 2001; Delescluse et al., 2012*].
463 Evidently the fracturing of the Indo-Australian plate is occurring by opportunistic
464 reactivation of weak zones in the lithosphere created by original faulting. Active fault
465 trends in both the NER and adjacent basins indicate that original fault azimuths, rather
466 than relative plate motion vectors (discussed in the next section) or other factors,
467 determine the pattern and direction of active faulting.

468 **4.2 Deformation within the NER and Implications for Diffuse Plate Boundaries**

469 It is expected that observed fault motion could be explained by relative plate motions
470 predicted by the three-plate model of *Royer and Gordon [1997]*, but with uncertainty
471 about the locations of plate boundaries and the response of the lithosphere to the stress
472 field implied by the plate motions. This model is based primarily on seafloor spreading
473 rates and fracture zone trends along central Indian Ocean mid-ocean ridges, which define
474 the plate-pair Euler poles (Fig. 1) [*DeMets et al., 2010; Bull et al., 2010*]. These poles
475 predict significant variations in relative motions along the NER (Fig. 19A). Predicted
476 motion at a given location depends on the angle that the relative motion vector makes
477 with the plate boundary as well as the assumed plate geometry. Only the most likely
478 combinations are shown in Figure 19A, where it is assumed that the India - Australia and
479 Capricorn - Australia boundaries trend N-S, but the India - Capricorn boundary strikes E-
480 W. Figure 19 shows only the direction of relative motion, but not the magnitude. The
481 amount of movement between the plates is small but greatest for the India-Australia pair
482 (total ~125 km). This is slightly more than twice that for India-Capricorn and roughly
483 five times as much as for Capricorn-Australia [*Royer and Gordon, 1997*]. Both India-
484 Australia and India-Capricorn Euler poles lie well off the NER, consistent with greater
485 amounts of relative motion (Fig. 1) and greater seismicity (Fig. 2). The Capricorn -
486 Australia Euler pole is near the southern end of the NER and its 95% confidence ellipse
487 encompasses Sites 253 and 756, so the magnitude of relative motion is small and the
488 direction of motion is uncertain at these sites.

489 **4.2.1 Northern NER (Sites 758 and 216)**

490 In the northern NER, prominent WNW-ESE bathymetric lineations are observed at
491 both Sites 758 and 216 and correspond to major active faults that display evidence of
492 strike-slip motion, often with local compression and sometimes extension. Deformation is
493 mostly strike-slip at both sites, consistent with the observed dominance of strike-slip
494 focal mechanisms for northern NER earthquakes (Fig. 2). Compression also occurs at
495 both sites; although, it appears greater at Site 758. Thus, the overall picture in the
496 northern NER is of transpression. Signs of extension occur at both sites, but it is minor in
497 nature. Extension probably occurs on releasing bends where the fault trend deviates from
498 being parallel to the direction of relative motion across the fault, a common feature of
499 strike-slip faults.

500 Although all three Euler poles imply NW-SE compression in the northern NER, it is
501 probable that this location is part of the India-Australia plate boundary (Figs. 1, 19)
502 [*Royer and Gordon, 1997*]. The Euler pole for this plate boundary implies compression
503 at an angle $\sim 45^\circ$ from the trend of the NER (Fig. 19A, C). This direction is oblique to
504 both the WNW-ESE transform faults observed in the NER and to the ENE-WSW
505 trending fracture zones that are reactivated in the Wharton Basin [*Deplus, 2001*;
506 *Delescluse et al., 2012*]. Because the oblique compression is $\sim 45^\circ$ from the trends of the
507 fracture zones, it makes about the same angle with original spreading-ridge normal faults.
508 Both sets of faults are oriented approximately along Riedel shear directions (Fig. 19C),
509 which likely results in opportunistic reactivation of these faults. Back-projection of the
510 April 2012 Wharton Basin earthquake aftershock pattern suggests that the fault ruptures

511 are not exactly parallel to the local magnetic lineations [*Meng et al., 2012*]. It is unclear
512 whether the small deviation in direction is significant or whether rupturing cuts across the
513 Strike-slip faults with N-S orientations are not observed in the areas of the northern
514 NER that were mapped with multibeam bathymetry data. This finding suggests that prior
515 interpretations of N-S strike-slip motion within the NER [*Stein and Okal, 1978; Petrov*
516 *and Wiens, 1989*] are incorrect. Because all observed tectonic lineations in the northern
517 NER are oriented nearly WNW-ESE, it is likely that strike-slip earthquake focal
518 mechanisms in the northern NER indicate motion with that trend. Our data do not cover
519 seafloor in adjacent basins where reactivated, ENE-WSW-oriented fracture zones may
520 exist, so we cannot tell how the NER and Wharton Basin faults connect.

521 Strike-slip motion observed within the northern NER is distinct from N-S
522 compression in the Central Indian Basin and ENE-WSW strike-slip in Wharton Basin.
523 These differences imply that this part of NER is indeed a tectonic discontinuity as
524 indicated by *Delescluse and Chamot-Rooke [2007]*. Because the aftershock distribution
525 related to the April 2012 Wharton Basin earthquake implies a “lattice” of intersecting
526 WNW-ESE and ENE-WSW strike-slip faults located on the east side of the NER [*Meng*
527 *et al., 2012*], it is possible that observed NER faulting is the western edge of that fault
528 pattern.

529 **4.2.2 Central NER (Sites NER2, NER3)**

530 At Sites NER2 and NER3, in the middle of the predicted diffuse triple junction (Fig.
531 1), active faulting documented by the seismic reflection data is dominantly thrusting on
532 E-W trending faults. Unfortunately, no earthquake focal mechanisms have been

533 produced from this portion of the NER (Fig. 2), so such data cannot inform this
534 interpretation. The observation of E-W oriented thrust faults implies N-S compressive
535 stress, which could be a result of either India-Australia or India-Capricorn motion as both
536 vectors have appropriate orientations (Fig. 19A). Capricorn-Australia relative motion is
537 nearly parallel to the observed faults, but significant strike-slip motion is not supported
538 by fault observations. Because these two sites are adjacent to the India-Capricorn
539 deformation zone and have a similar style and direction, the observed Site NER2-NER3
540 faulting may linked to that in the Central Indian Basin deformation. However, India-
541 Australia relative motion is also plausible as a driver of faulting at this site. An important
542 difference from the Central Indian Basin is that thrust faults at NER2-NER3 have small
543 offsets, but those nearby in the Central Indian Basin can be much larger [*Bull and*
544 *Scrutton, 1992*], implying greater strain accumulation in the adjacent basin.

545 Evidence of strike-slip motion is observed on some faults within NER2-NER3,
546 suggesting that the relative motion at these sites includes a component parallel to the
547 faults. Strike-slip motion may occur because the relative motion vectors are not-quite
548 perpendicular to the E-W trend of spreading-ridge-formed precursor faults (Fig. 19C). If
549 true, this observation supports the idea that original fault sets localize deformation with
550 recent motions having components both parallel and perpendicular to the fault.

551 **4.2.3 Southern NER (Sites 214, 757, 253, and 756)**

552 In the northern and central NER, observed faulting is well-explained by the
553 predicted relative motions of the three plate system [*Royer and Gordon, 1997*]. In the
554 southern NER, the translation of relative plate motions into faulting is less clear. One
555 element of uncertainty is the significant shift in plate motions caused by the proximity of

556 the Capricorn-Australia pole to the southernmost NER and the fact that the NER crosses
557 from a region of extension to compression in the velocity field of the India-Australia
558 pole. The former situation means that the magnitude of relative motion changes rapidly
559 along the southern NER and the direction is highly uncertain. The latter causes relative
560 motion along a either N-S or E-W oriented faults to shift from convergence north of
561 $\sim 11^\circ\text{S}$ to extension farther south (Fig. 19A, compare Site NER2-NER3 to Site 214).

562 Faults observed in seismic sections at both Sites 214 and 253, at the north and south
563 ends of the high, linear section of the southern NER, mostly have a normal geometry.
564 Data from Sites 757 and 756 are of low quality and do not clearly show the geometry of
565 most observed faults. Although these data are consistent with observations at Sites 214
566 and 253, we base our interpretations on data from the two recently-surveyed sites.
567 Normal faulting is dominant at both sites, but displacement on active faults appears
568 small, indicating low strain. A few faults at each site show characteristics of possible
569 compression or strike-slip motion. The non-normal faults appear clustered, implying
570 zones of compression or strike-slip motion surrounded by normal faulting. This mixture
571 of fault types suggests that faulting in the southern NER is complex and possibly
572 incompletely defined by the small areas of seismic reflection data available.

573 Normal faulting is unexpected in the southern NER, given that the three focal
574 mechanisms located on this part of the ridge show thrust faulting and strike-slip
575 mechanisms occur in adjacent basins (Fig. 2). Relative plate motions for this part of the
576 NER should be described by the Capricorn-Australia Euler pole (Fig. 1). Although this
577 pole predicts extension for Site 756, it implies compression, not extension, from Site 253
578 northward (Fig. 19A). Both sites lie within the 95% confidence ellipse of the pole, so

579 relative motion predictions are uncertain for these sites. However, if the Euler pole is
580 actually located slightly farther north, then extension is expected at both sites (Fig. 19C),
581 which are then part of a zone of extension extending southwest from the southern NER
582 [*Royer and Gordon, 1997*] (Fig. 19B). Because of the proximity of the pole and its low
583 rotation rate [*Royer and Gordon, 1997*], relative motion between the two plates in this
584 area should be very small, but this is consistent with the low strain on observed faults.

585 According to Royer and Gordon [1997], Site 757 is located within the Capricorn-
586 Australia boundary whereas Site 214 is at the junction of that boundary with the diffuse
587 triple junction (Fig. 1). The Capricorn-Australia pole predicts convergence nearly
588 perpendicular to the NER at both locations. Although this prediction is consistent with
589 the thrust fault focal mechanism recorded near Site 757, it does not explain the
590 prevalence of normal faults in seismic sections. In contrast, the India-Australia pole
591 predicts extension at both sites (Fig. 19A), whether or not a fault is oriented N-S or E-W.
592 The abrupt shift from convergence at Site NER2-NER3 to extension at Site 214 could be
593 a result of the former being north of the India-Australia Euler pole and the latter being to
594 the south. For N-S trending faults, the change is small because the relative motion vector
595 has nearly the same orientation, but for E-W oriented faults, the shift is from nearly
596 perpendicular compression to extension.

597 Site 757 is located on a section of the NER that is too far south to be plausibly a part
598 of the India-Australia boundary. Because seismic data are unclear at this site, it is
599 possible that the observed active faulting is compression caused by Capricorn-Australia
600 motion, an interpretation consistent with the thrust focal mechanism located nearby (Fig.
601 2).

602 **4.2.4. Tectonic Overview**

603 We observe that active faulting within the NER is opportunistic, reactivating original
604 faults mostly in response to regional relative plate motions. It does not seem to matter
605 that the original fault fabric is often at a significant angle from the relative motion
606 vectors, the original faults are weak and therefore break before intact crust. Because the
607 regional stress pattern and relative plate motions are both usually oblique to the fault
608 fabric, many active faults appear to have complex motion. In the northern NER, original
609 normal faults are reactivated mainly as strike-slip faults, but with a component of
610 compression (Fig. 19C, Sites 758, 216). In the central NER, a shift in relative motion
611 directions causes reactivation of early normal faults with mostly compressive motion, but
612 with a component of strike-slip (Fig. 19C, Sites NER2-NER3). The relationship of
613 broad-scale plate motions to active faulting in the southern NER is more complex.
614 Faulting appears a mixture, with widespread extension punctuated with compression or
615 strike-slip motion. This apparent paradox suggests that the southern NER has narrow
616 zones of deformation responding to the regional plate motions with surrounding areas of
617 slight extension. Extension at Sites 253 and 756 may be explained by inclusion in a zone
618 of Capricorn-Australia divergence south of the Euler pole for that plate pair (Fig. 19B).
619 Site 214 is interesting because it shows a dramatic shift from the compressional
620 deformation occurring only a few degrees of latitude farther north at Site NER2-NER3.
621 Given that fault motions at Sites NER2-NER3 and 214 can be explained by the India-
622 Australia pole, we favor the explanation that the NER north of $\sim 11^\circ\text{S}$ is part of the
623 boundary of that plate pair. This abrupt shift could instead represent a more complex
624 blending of deformation in the diffuse triple junction, but we have insufficient data to

625 support an explanation of greater complexity. Interestingly, the difference between Sites
626 NER-NER3 and 214 is also apparent in the active strain model of *Delescluse and*
627 *Chamot-Rooke* [2007], derived from earthquake focal mechanisms and geodetic GPS
628 measurements. This model shows strong, NNW-SSE compression in the central NER
629 from 3°-8°S, but only slight strain south of 8°S. The maximum strain axis direction near
630 Sites NER2-NER3 is coincident with India-Australia motion (Fig. 19A), suggesting this
631 portion of the NER is associated with that boundary.

632 No clear seismic data are available from the ~15° of the southern NER surrounding
633 Site 757. Although existing data show that faulting is occurring at that site, the type of
634 faulting is uncertain. Because earthquake focal mechanisms and the strain model
635 [*Delescluse and Chamot-Rooke, 2007*] indicate oblique compression approximately
636 coincident with expected Capricorn-Australia motion, it is likely that faulting in this zone
637 is mainly thrust faulting related to the convergence of these two plates.

638 It is clear from seismic data that changes in the style of faulting occur along the
639 NER, sometimes abruptly. Sites 216 and NER2 are separated by ~7° (~780 km) and the
640 mostly strike-slip style of faulting at Sites 758 and 216 is dramatically different from the
641 primarily thrust fault deformation at Sites NER2 and NER3. Between Sites NER3 and
642 214, separated by only ~2.5° (~260 km), there is an abrupt change from mainly thrust
643 faulting to mainly normal faulting. In addition, several sites (NER3, 214, 253) show
644 evidence of mixed faulting. These changes probably occur because the pre-existing fault
645 fabric at different locations responds to regional changes in relative plate motions and
646 stress orientations. Faulting sometimes appears to change more abruptly than expected

647 from the broad shifts in relative motion implied by the three-plate model, an indication
648 that pre-existing structure is an important factor in the fracturing of the plates.

649 Changes in fault style indicate that the NER crosses at least two different diffuse
650 boundaries. The northern NER (Sites 214, NER2-NER3, 216, and 758) appears to show
651 deformation related to the India-Australia plate boundary, whereas the southern NER
652 (Sites 757, 253, 756) shows Capricorn-Australia motion. It is also possible that the
653 diffuse triple junction is more complex and also shows India-Capricorn motion (i.e., Site
654 NER2-NER3). If the NER does not cross the India-Capricorn boundary, it cannot be far
655 away because the thrust faulting in this zone has been observed directly adjacent to the
656 northern NER (Fig. 19B; [Weissel *et al.*, 1980; Bull and Scrutton, 1992]). Such an abrupt
657 change from one relative motion to another is consistent with the observed abrupt change
658 in earthquake style and with deformation models derived from earthquake motion
659 [Deplus, 2001; Delescluse and Chamot-Rooke, 2007].

660 **5. Conclusions**

661 Analyses of seismic reflection data shows that active faulting is found along the
662 entire ~4500 km length of the NER, but with variable intensity and style depending on
663 location relative to diffuse plate boundaries and relative plate motion Euler poles. At all
664 sites, recent deformation has reactivated spreading-center-formed normal faults.
665 Together with similar results in adjacent basins, this finding implies that Indo-Australian
666 plate fracturing occurs mainly by reactivation of faults formed at the time of lithosphere
667 creation. Fault directions are observed to correspond to the original structure rather than
668 the regional plate motion pattern, indicating that pre-existing structure is the most
669 important factor determining fault geometry.

670 In the northern NER (north of 1.5°N), the dominant deformation style is
671 transpression on faults having a WNW-ESE trend. The observed direction of strike-slip
672 motion is unexpected because prior interpretations of earthquake focal mechanisms
673 within the northern NER were interpreted to support N-S strike-slip, consistent with
674 reactivation of ancient fracture zones in the nearby Wharton Basin. Apparently NW-SE
675 compression within the India-Australia diffuse plate boundary reactivates original
676 spreading-center normal faults in the NER and fracture zones in the Wharton Basin along
677 oblique Riedel shear directions.

678 In the central NER (6.7° - 7.7°S), deformation shifts to predominantly thrust faulting,
679 similar to that observed in the Central Indian Basin, perhaps with a minor amount of
680 strike-slip motion. Although this deformation could result from either India-Capricorn or
681 India-Australia relative motion, the latter is a simpler explanation because it agrees with
682 interpretations of sites to the north and south. A few faults show evidence of strike-slip
683 motion, suggesting that the stress pattern applied by regional plate motions has a
684 component parallel to the original faults.

685 Deformation style again changes abruptly between 7.7°S to 11.3°S . Southern NER
686 deformation is modest and is expressed mainly as normal faulting, but interrupted by
687 zones of strike-slip or compressional faulting. Extension at the southernmost end of the
688 NER is explained as part of a zone of Capricorn-Australia divergence south of that Euler
689 pole, whereas extension at 11.3°S is explained as part of the India-Australia boundary, as
690 are sites farther north. Although low-resolution seismic data in the gap between these
691 areas show active faulting, the style of faulting is unclear but likely to be Capricorn-
692 Australia convergence consistent with observed thrust fault focal mechanisms.

693 Seismic data from the NER indicate that diffuse deformation is widespread and often
694 complex, sometimes with mixtures of different fault types suggesting interplay of
695 regional stresses and pre-existing structures. Our interpretation is that the northern NER
696 shows India-Australia relative motion whereas the southern NER responds to Capricorn-
697 Australia motion. India-Capricorn deformation has been documented to the western edge
698 of the NER, implying that changes in deformation style can be abrupt. This observation
699 agrees with published findings that the northern NER is a break between deformation
700 fields on either side. Although observed deformation can be understood by the
701 framework of larger plate motions, faulting is more complex than existing plate models
702 predict.

703 **Acknowledgments.**

704 We thank captain Tom Desjardins, seismic technicians Lee Ellett and Brandi Reese,
705 and the crew of the R/V *Roger Revelle* during cruise KNOX06RR for making data
706 collection possible. We are indebted to Amy Eisin for seismic data processing and Chris
707 Paul, for bathymetry data processing. We thank Halliburton/Landmark for use of
708 *ProMAX* software and Seismic Micro Technology for use of *Kingdom Suite* software.
709 We are appreciative of two anonymous reviewers, who provided thorough and challenging
710 reviews that helped strengthen our analysis. This project was funded by the National
711 Science Foundation (grants OCE- 0550743 and OCE-0549852).

712 **References**

- 713 Bull, J. M., C. DeMets, K. S. Krishna, D. J. Sanderson, and S. Merkouriev (2010),
714 Reconciling plate kinematic and seismic estimates of lithospheric convergence in the
715 central Indian Ocean, *Geology*, *38*, 307-310, doi:10.1130/G30521.1.
- 716 Bull, J. M., and R. A. Scrutton (1990), Fault reactivation in the central Indian Ocean and
717 the rheology of oceanic lithosphere, *Nature*, *344*, 855-858.
- 718 Bull, J. M., and R. A. Scrutton, R. A. (1992), Seismic reflection images of intraplate
719 deformation, central Indian Ocean, and their tectonic significance, *Geol. Soc. London*
720 *J.*, *149*, 955-966, doi: 10.1144/gsjgs.149.6.0955.
- 721 Cande, S. C., and D. V. Kent (1995), Revised calibration of the geomagnetic polarity
722 timescale for the Late Cretaceous and Cenozoic, *J. Geophys. Res.*, *100*, 6093-6095.
- 723 Curray, J. S., and T. Munasinghe (1989), Timing of intraplate deformation, northeastern
724 Indian Ocean, *Earth Planet. Sci. Lett.*, *94*, 71-77.
- 725 Delescluse, M., and N. Chamot-Rooke (2007), Instantaneous deformation and kinematics
726 of the India-Australia plate, *Geophys. J. Int.*, *168*, 818-842, doi: 10.1111/j.1365-
727 246X.2006.03181.x.
- 728 Delescluse, M., L. G. J. Montési, and N. Chamot-Rooke (2008), Fault reactivation and
729 selective abandonment in the oceanic lithosphere, *Geophys. Res., Lett.*, *35*, 1-5,
730 doi:10.1029/2008GL035066.
- 731 DeMets, D., R. G. Gordon, and D. F. Argus (2010), Geologically current plate motions:
732 *Geophys. J. Int.*, *181*, 1-80, doi: 10.1111/j.1365-246x.2009.04491.x.
- 733 Deplus, C. (2001), Indian Ocean actively deforms, *Science*, *292*, 1850-1851, doi:
734 10.1126/science.1061082.

735 Deplus, C., M. Diament, H. Hébert, G. Bertrand, S. Dominguez, J. Dubois, J. Malod, P.
736 Patriat, B. Pontoise, and J. J. Sibilla (1998), Direct evidence of active deformation in
737 the eastern Indian oceanic plate, *Geology*, 26, 131-134.

738 Flueh, C., and C. Reichert (1998), *Cruise report SO131, SINUS – seismic investigations*
739 *at the Ninetyeast Ridge observatory using SONNE and JOIDES RESOLUTION*
740 *during ODP Leg 179*, GEOMAR Rept. 72, Kiel, Germany, 377 pp.

741 Gordon, R. G. (2000), Diffuse oceanic plate boundaries: Strain rates, vertically averaged
742 rheology, and comparisons with narrow plate boundaries and stable plate interiors, *in*
743 *The History and Dynamics of Global Plate Motions*, edited by M. A. Richards, R. G.
744 Gordon, and R. D. van der Hilst, R. D., Geophysical Monograph v. 121. pp. 143-159,
745 AGU, Washington, DC.

746 Grevenmeyer, I., E. R. Flueh, C. Reichert, J. Bialas, D. Kläschen, and C. Kopp (2001),
747 Crustal architecture and deep structure of the Ninetyeast Ridge hotspot trail from
748 active-source ocean bottom seismology, *Geophys. J. Int.*, 144, 414-431.

749 International Seismological Centre (2013), On-line Bulletin, <http://www.isc.ac.uk>, Seis.
750 Cent., Thatcham, United Kingdom.

751 Krishna, K. S., H. Abraham, W. W. Sager, M. S. Pringle, F. Frey, D. Gopala Rao, and O.
752 V. Levchenko (2012), Tectonics of the Ninetyeast Ridge derived from spreading
753 records in adjacent ocean basins and age constraints of the ridge, *J. Geophys. Res.*,
754 117, doi:10.1029/2011JB008805.

755 Krishna, K. S., J. M. Bull, and R. A. Scrutton (2001), Evidence for multiphase folding of
756 the central Indian Ocean lithosphere, *Geology*, 29, 715–718, doi:10.1130/0091-
757 7613(2001).

758 Krishna, K. S., J. M. Bull, and R. A. Scrutton (2009), Early (pre-8 Ma) fault activity and
759 temporal strain accumulation in the central Indian Ocean, *Geology*, *37*, 27-230.

760 Krishna, K. S., D. Gopala Rao, M. V. Ramana, V. Subrahmanyam, K. V. L. N. S. Sarma,
761 A. I. Pilipenko, V. S. Scherbakov, and I. V. Radhakrishna Murthy (1995), Tectonic
762 model for the evolution of oceanic crust in the northeastern Indian Ocean from the
763 Late Cretaceous to early Tertiary, *J. Geophys. Res.*, *100*, 20,011-20,024.

764 McGuire, J. J., and G. C. Beroza, (2012), A rogue earthquake off Sumatra, *Science*, *336*,
765 1118-1119.

766 Meng, L., J.-P. Ampuero, J. Stock, Z. Duputel, Y. Luo, and V. C. Tsai (2012),
767 Earthquake in a maze: Compressional rupture branching during the 2012 Mw 8.6
768 Sumatra earthquake, *Science*, doi:10.1126/science.1224030.

769 Naini, B. R., and S. L. Eittreim (1974), Appendix II. Marine geophysical survey (Site 214
770 DSDP) on the Ninetyeast Ridge, Indian Ocean, *Init. Repts. DSDP*, *22*, 843-849.

771 Newman, J. S., and J. G. Sclater (1988), Site surveys of the central and southern
772 Ninetyeast Ridge for the Ocean Drilling Program, Leg 121, UTIG Technical Rept. 74,
773 University of Texas, Austin, TX, 137 pp.

774 Norton, I. O., and J. G. Sclater (1979), A model for the evolution of the Indian Ocean and
775 the breakup of Gondwanaland, *J. Geophys. Res.*, *84*, 6803-6830.

776 Petroy, D. E., and D. A. Wiens (1989), Historical seismicity and implications for diffuse
777 plate convergence in the northeast Indian Ocean, *J. Geophys. Res.*, *94*, 12,301-12,319.

778 Pilipenko, A. I. (1996), Fracture zones of the Ninetyeast Ridge area, Indian Ocean,
779 *Geotectonics*, *30*, 441-451.

780 Robinson, D. P., C. Henry, S. Das, and J. H. Woodhouse (2001), Simultaneous rupture
781 along two conjugate planes of the Wharton Basin earthquake, *Science*, 292, 1145-
782 1148.

783 Royer, J.-Y., and Gordon, R. G. (1997), The motion and boundary between the Capricorn
784 and Australian plates, *Science*, 277, 268-1274.

785 Royer, J.-Y., J. W. Peirce, and J. K. Weissel (1991), Tectonic constraints on the hot-spot
786 formation of Ninetyeast Ridge, *Proc. ODP, Sci. Res.*, 121, 763-776.

787 Royer, J.-Y., and D. T. Sandwell (1989), Evolution of the eastern Indian Ocean since the
788 Late Cretaceous: Constraints from Geosat altimetry, *J. Geophys. Res.*, 94, 13,755-
789 13,782.

790 Sager, W.W. et al. (2007), Cruise Report KNOX06RR R/V Roger Revelle, 82 pp.
791 (<http://earthref.org/erda/1172>).

792 Sager, W. W., C. F. Paul, K. S. Krishna, M. S. Pringle, A. E. Eisin, F. A. Frey, D. Gopala
793 Rao, and O. Levchenko (2010), Large fault fabric of the Ninetyeast Ridge implies
794 near-spreading ridge formation, *Geophys. Res. Lett.*, 37, doi:10.1029/
795 2010GL044347.

796 Satriano, C., E. Kiraly, P. Bernard, and J.-P. Vilotte (2012), The 2012 Mw 8.6 Sumatra
797 earthquake: Evidence of westward sequential seismic ruptures associated to the
798 reactivation of a N-S ocean fabric, *Geophys. Res. Lett.*, 39,
799 doi:10.1029/2012GL052387.

800 Shipboard Scientific Party (1974), Site 253, *Init. Repts. DSDP*, 26, 153-231.

801 Shipboard Scientific Party (1989a), Ninetyeast Ridge underway geophysics, *Proc. ODP*,
802 *Init. Repts.*, 121, 93-107.

803 Shipboard Scientific Party (1989b), Back pocket foldouts, *Proc. ODP, Init. Repts*, 121.

804 Smith, W. H. F., and D. T. Sandwell (1997), Global sea floor topography from satellite
805 altimetry and ship depth soundings, *Science*, 277, 1956–1962.

806 Stein, C. A., S. Cloetingh, and R. Wortel (1990), Kinematics and mechanics of the Indian
807 Ocean diffuse plate boundary zone, *Proc. ODP. Sci. Res.*, 116, 261-277.

808 Stein, C., S. Cloetingh, and R. Wortel (1989), Seasat-derived gravity constraints on stress
809 and deformation in the northeastern Indian Ocean, *Geophys. Res. Lett.*, 16, 823-826.

810 Stein, S., and E. A. Okal (1978), Seismicity and tectonics of the Ninetyeast Ridge area:
811 evidence for internal deformation of the Indian Plate, *J. Geophys. Res.*, 83, 2233-
812 2245.

813 Tinnon, M. J., W. E. Holt, and A. J. Haines (1995), Velocity gradients in the northern
814 Indian Ocean inferred from earthquake moment tensors and relative plate velocities,
815 *J. Geophys. Res.*, 100, 24,315-24,329.

816 Veevers, J. J. (1974), Seismic profiles made underway on Leg 22, *Init. Repts. DSDP*, 22,
817 351-367.

818 Weissel. J. K., R. N. Anderson, and C. A. Gellar (1980), Deformation of the Indo-
819 Australian plate, *Nature*, 287, 284-291.

820 Wiens, D. A., S. Stein, C. DeMets, R. G. Gordon, and C. Stein (1986), Plate tectonic
821 models for Indian Ocean "intraplate" deformation, *Tectonophysics*, 132, 37-48.

822

823

824 **Figure Captions**

825 Figure 1. Ninetyeast Ridge environs and tectonic setting. Background plot is satellite-
826 predicted bathymetry [*Smith and Sandwell, 1997*]. Shaded areas around the NER
827 represent diffuse plate boundaries (I-C=India-Capricorn, C-A=Capricorn-Australia, I-
828 A=India-Australia; DTJ=diffuse triple junction) [*Royer and Gordon, 1997*]. Stippled
829 zone northwest of the NER indicates the area of lithospheric compression resulting from
830 India-Capricorn convergence [*Krishna et al., 2001; 2009*]. Red boxes show study sites.
831 Red-filled circles denote Euler poles: IN-CP =India-Capricorn, IN-AU=India-Australia,
832 CP-AU=Capricorn-Australia [*DeMets et al., 2010*]. Red ellipses show pole 95%
833 confidence regions. Red filled square is updated IN-CP pole from *Bull et al. [2010]*.
834 ASP=Amsterdam-St. Paul Plateau; BR=Broken Ridge; CR=Carlsberg Ridge;
835 CLR=Chagos-Laccadive Ridge; JT=Java Trench; SEIR=Southeast Indian Ridge.

836 Figure 2. Earthquakes in the Ninetyeast Ridge vicinity. Left panel shows epicenters from
837 1970-2012 with symbols scaled with body-wave magnitude (scale at bottom). Right
838 panel shows focal mechanisms for the same period. Background is satellite-predicted
839 bathymetry [*Smith and Sandwell, 1997*]. Data source: *International Seismological*
840 *Centre (2013)*.

841 Figure 3. Shaded relief bathymetry and tectonic interpretation maps of the Site 758
842 survey. High detail area is covered with multibeam echosounder data, whereas low-
843 resolution data are satellite predicted depths [*Smith and Sandwell, 1997*]. (left)
844 Bathymetry. Thin black lines are seismic lines. Open circle shows location of ODP Site
845 758. Bathymetry contours are at 200-m intervals and contour labels are in km. (right)
846 Tectonic interpretation. Red dashed lines show bathymetric lineaments. Blue lines

847 highlight contours with sharp bends. Faults observed in seismic profiles are marked by
848 symbols along seismic track lines; gray symbols denote less certain interpretations.
849 Circled letters identify seismic lines in Figure 4 whereas white track segments denote the
850 extent of the seismic profiles shown in that figure.

851 Figure 4. Seismic line examples showing active faults from the Site 758 survey. Seismic
852 sections plot two-way travel time versus distance. Arrows mark faults. Gray arrows
853 denote probable, but less certain fault interpretations. Locations of seismic sections are
854 shown in Figure 3 (letters A, B, C denote line segments labeled in that figure). Numbers
855 identify faults mentioned in the text.

856 Figure 5. Fault interpretation map for single-channel seismic data from cruise RC2705
857 near ODP Site 758. Fault symbols are plotted on seismic lines. High-resolution
858 bathymetry covers the area shown in Figure 3. White line shows the location of the
859 seismic line shown in Figure 6. Low-resolution bathymetry contours are from satellite
860 predicted bathymetry [*Smith and Sandwell, 1997*].

861 Figure 6. Single channel seismic profile from R/V *Robert Conrad* cruise RC2705.
862 Conventions as in Figure 4.

863 Figure 7. Shaded relief bathymetry map (left) and tectonic interpretation (right) of the
864 Site 216 survey. White lines denote seismic profiles shown in Figure 8. Open circle
865 shows location of ODP Site 216. Blue stars show locations of aftershock epicenters
866 associated with the 11 April 2012 Wharton Basin earthquake.

867 Figure 8. Seismic line examples showing active faults from the Site 216 survey.
868 Conventions as in Figure 4. Locations of seismic sections shown in Figure 7.

869 Figure 9. Shaded relief bathymetry map (left) and tectonic interpretation (right) of the
870 Site NER2 survey area. White lines denote seismic profiles shown in Figure 10.

871 Figure 10. Seismic line examples showing active faults from the Site NER2 survey.
872 Conventions as in Figure 4. Locations of seismic sections shown in Figure 9.

873 Figure 11. Shaded relief bathymetry map (left) and tectonic interpretation (right) of the
874 Site NER3 survey. White lines denote seismic profiles shown in Figure 12.

875 Figure 12. Seismic line examples showing active faults from the Site NER3 survey.
876 Conventions as in Figure 4. Locations of seismic sections shown in Figure 11.

877 Figure 13. Shaded relief bathymetry map (left) and tectonic interpretation (right) of the
878 Site 214 survey. White lines denote seismic profiles shown in Figure 14. Open circle
879 shows location of Site 214.

880 Figure 14. Seismic line examples showing active faults from the Site 214 survey.
881 Conventions as in Figure 4. Locations of seismic sections shown in Figure 13.

882 Figure 15. Shaded relief bathymetry around Site 757 (left) and Site 756 (right) and fault
883 interpretations from single-channel seismic data. Heavy line shows ship track of cruises
884 RC2708 (left) and RC2707 (right). Site 757 bathymetry data are multibeam data from
885 R/V *Sonne* [Flueh and Richert, 1998]. Dashed line in Site 757 survey shows ship track
886 for seismic data collected by the D/V *JOIDES Resolution* during ODP Leg 121
887 [Shipboard Scientific Party, 1989a; 1989b]. Site 756 bathymetry is predicted from

888 satellite gravity [Smith and Sandwell, 1997]. Interpreted fault symbols are as in other
889 figures (see Figure 3). White portions ship tracks are profiles shown in Figure 16.

890 Figure 16. Single channel seismic profiles from R/V *Robert Conrad* cruises RC2707 and
891 RC2708. Conventions as in Figure 4.

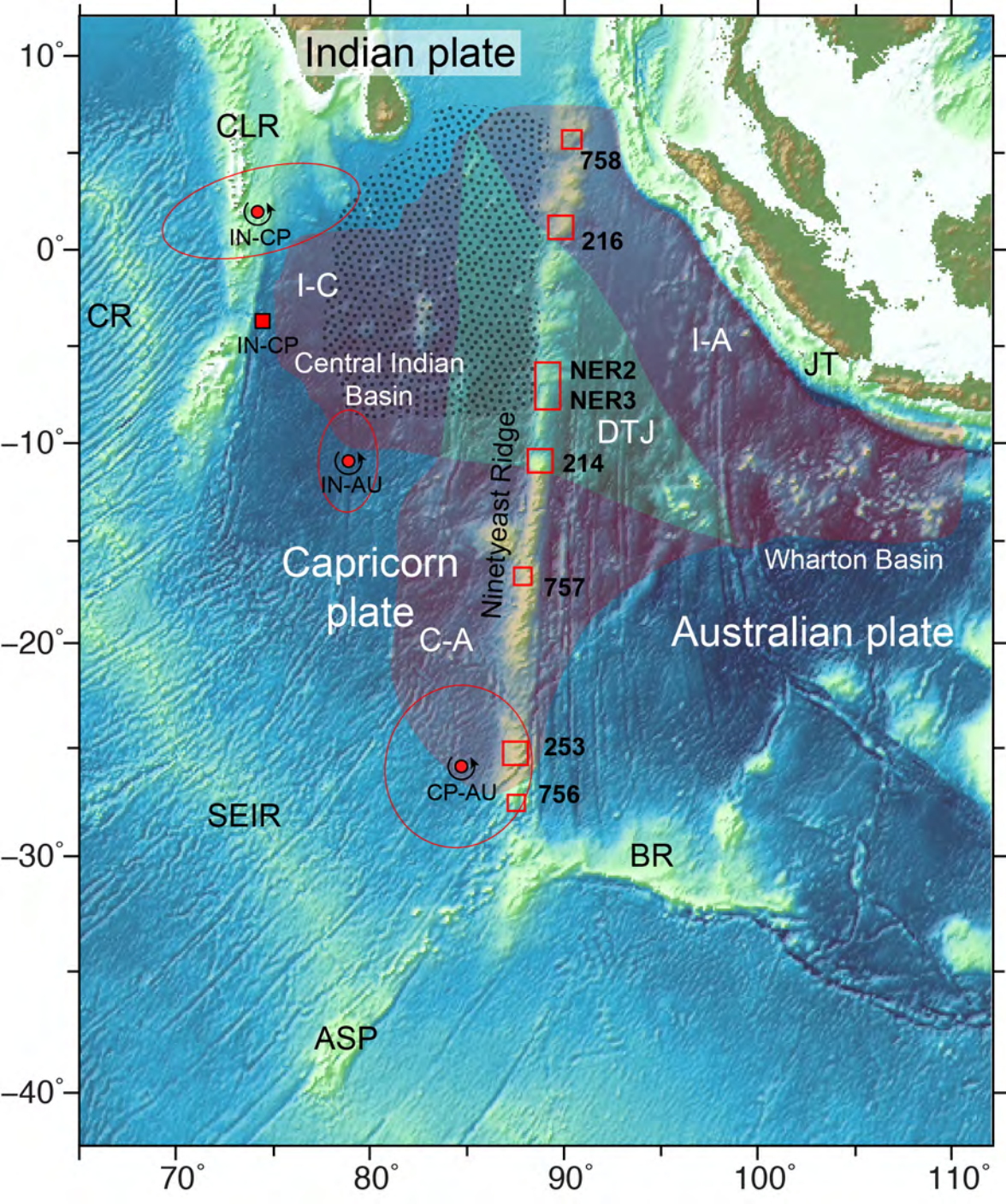
892 Figure 17. Shaded relief bathymetry (left) and tectonic interpretation (right) maps of the
893 Site 253 survey. White lines show seismic profiles shown in Figure 18. Open circle
894 shows location of Site 253.

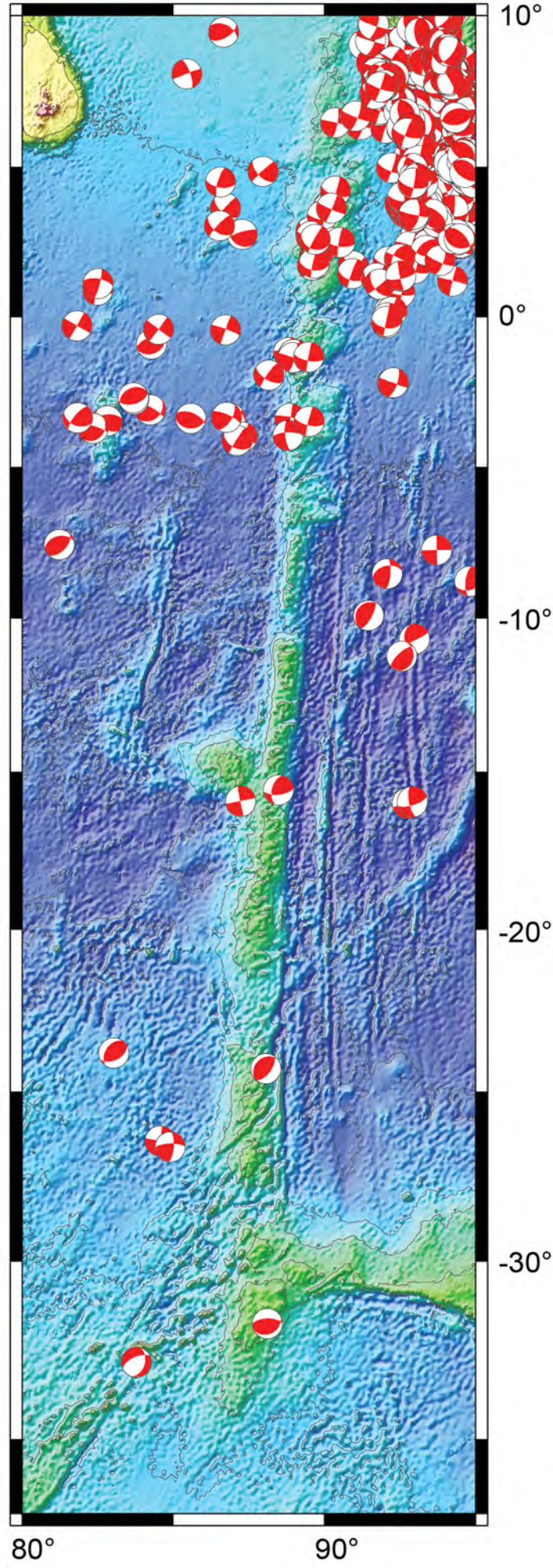
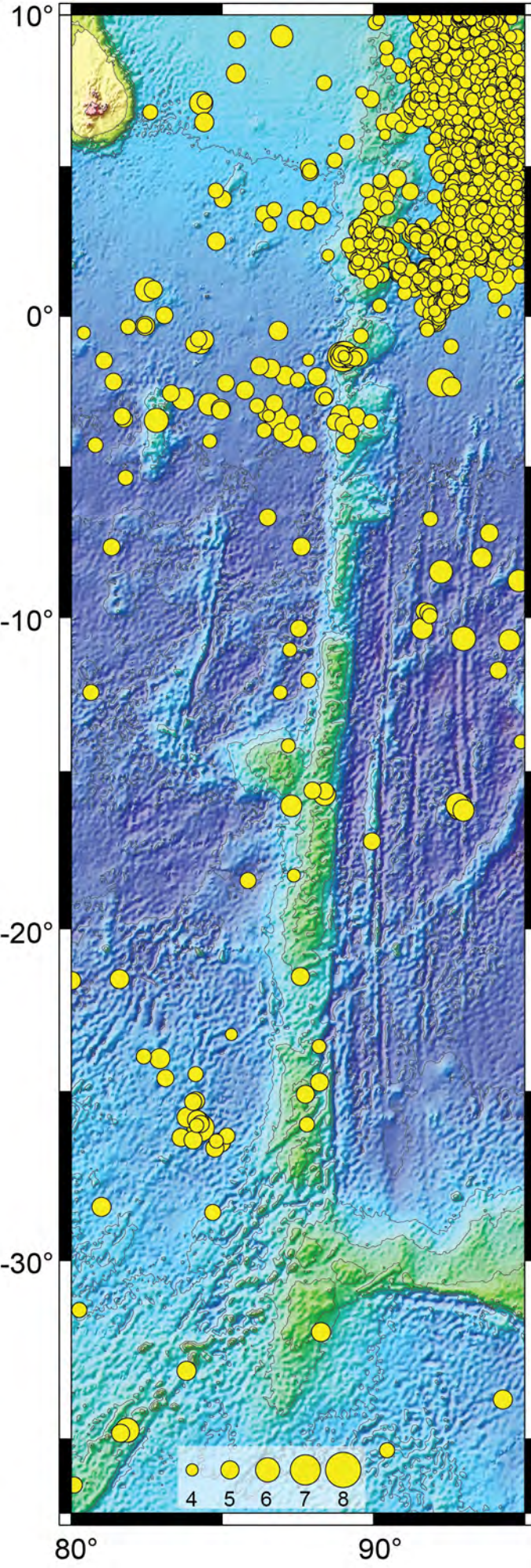
895 Figure 18. Seismic line examples showing active faults from the Site 253 survey.
896 Conventions as in Figure 4. Locations of seismic sections shown in Figure 17.

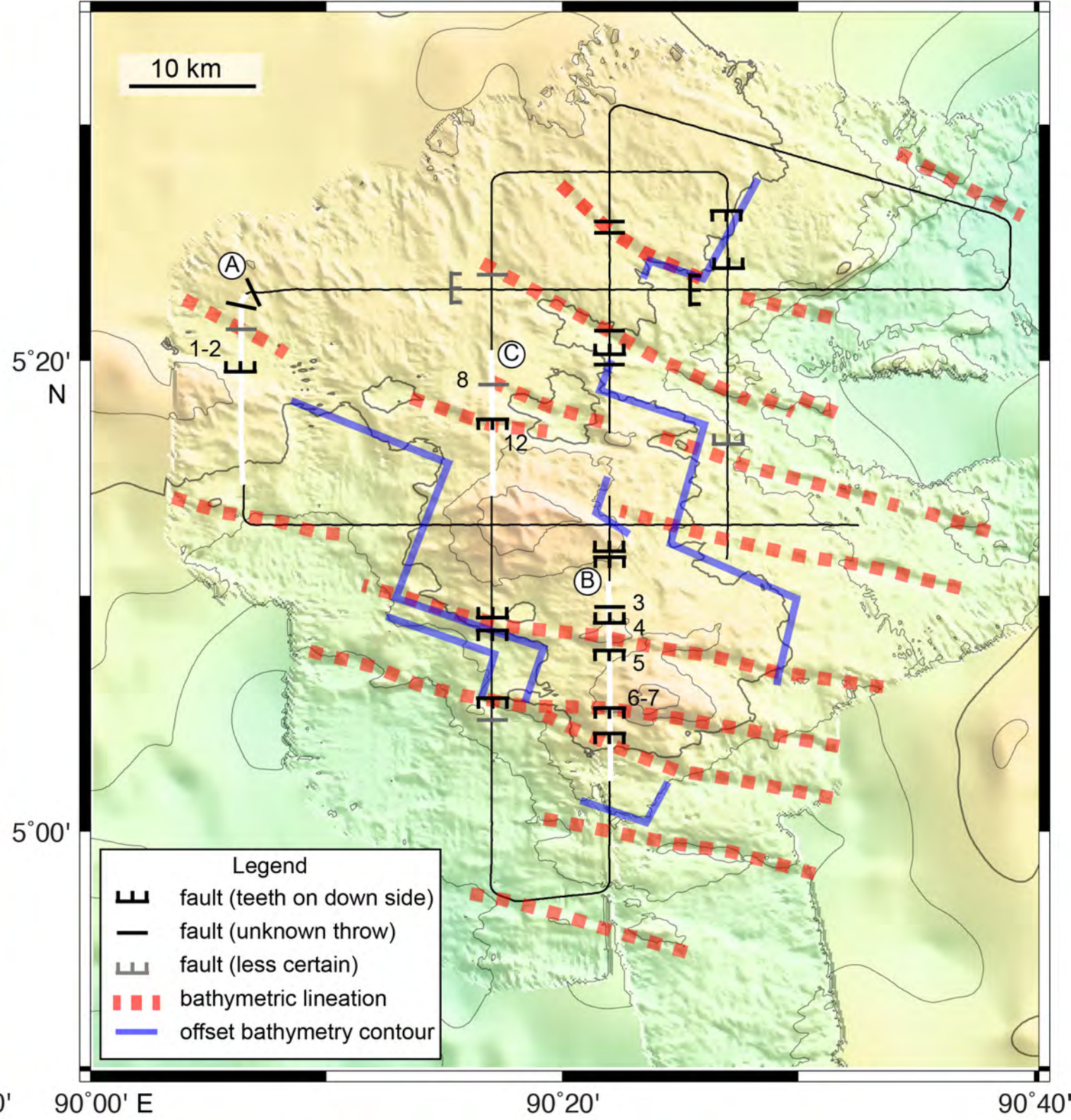
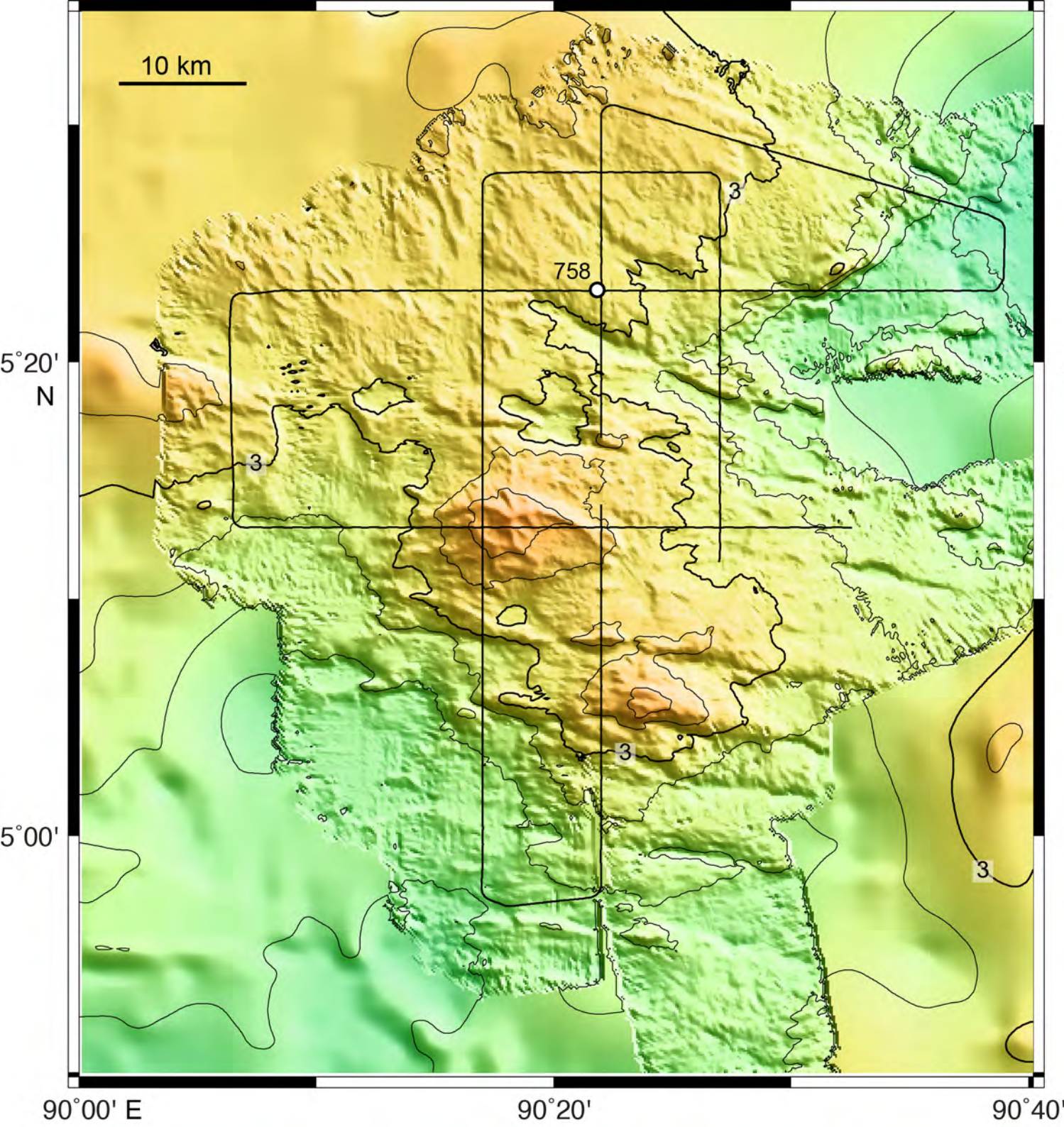
897 Figure 19. Tectonic sketch of relative plate motions, plate boundaries, and inferred fault
898 motions for the Ninetyeast Ridge. (A) Relative plate motions calculated from plate pair
899 Euler poles [DeMets et al., 2010]. Arrows show azimuth and sense of motion. Inward
900 pointing arrows denote compression whereas outward-pointing arrows indicate extension.
901 Black arrows show Capricorn-Australia motion (C-A), middle gray arrows represent
902 India-Australia motion (I-A), and light gray arrows show India-Capricorn motion (I-C).
903 To infer extension and convergence, the plates are assumed to have the configuration
904 shown in Figure 1 with the India-Australia and Capricorn-Australia boundaries oriented
905 N-S but the India-Capricorn boundary trending E-W. In the northernmost NER,
906 Capricorn-Australia motion is not shown because this is an unlikely pairing in this area.
907 The same is true for India-Australia at the southernmost sites. (B) Sketch of plate
908 boundaries around the NER. The large dot pattern shows the zone of India-Capricorn
909 compression [Krishna et al., 2001; 2009], the stippled area denotes the India-Australia

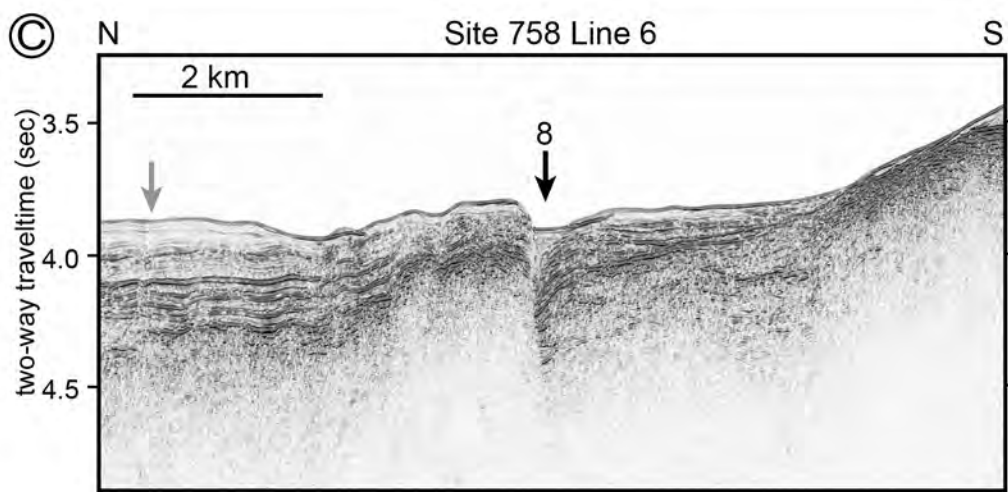
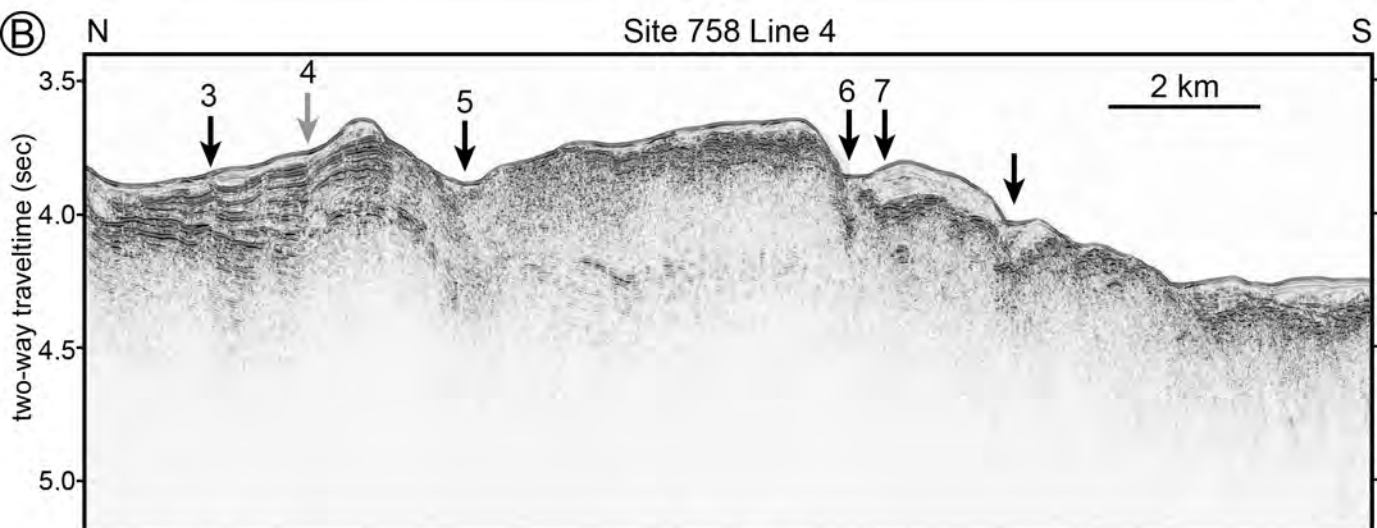
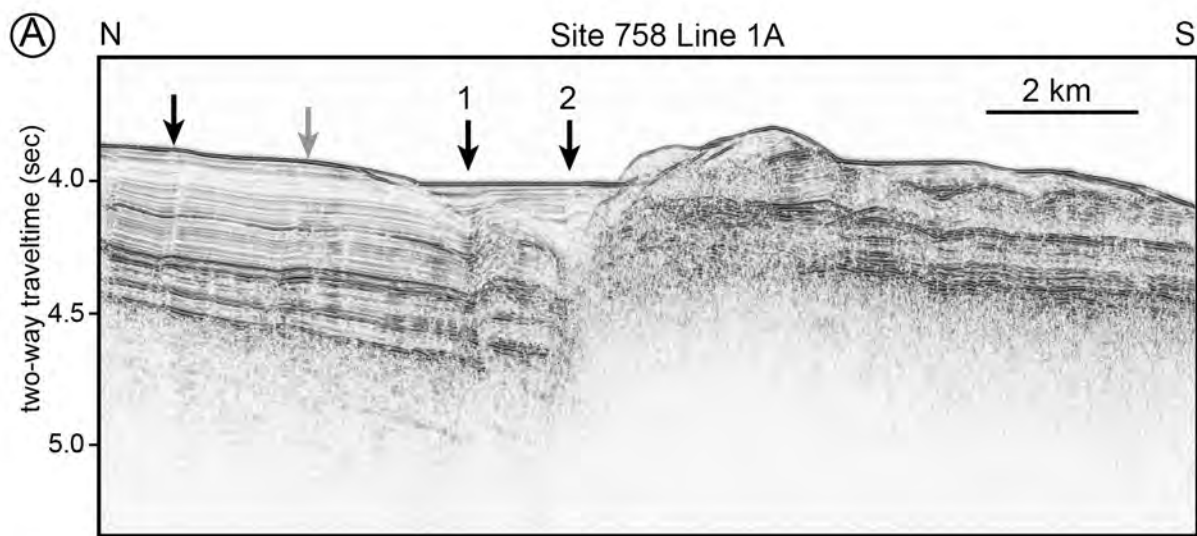
910 boundary, and large and small dot patterns indicates the Capricorn-Australia boundary
911 with the latter being a zone of extension and the former, a zone of compression [*Royer*
912 *and Gordon, 1997*]. Arrows indicate relative motions predicted by the three plate model.
913 (C) Fault interpretations at survey sites. Boxed diagrams illustrate relative plate motions
914 at the study sites and the fault response. Numbers are site identifiers. The horizontal
915 dashed line represents an E-W fault. Heavy arrows indicate plate motions predicted by
916 three-plate model (IN=India, CP=Capricorn, AU=Australia; *Royer and Gordon [1997]*).
917 Small arrows indicate motions along the faults; dark arrows denote the sense of primary
918 motion and gray arrows represent secondary sense of motion. Elliptical diagram for Sites
919 758-216 shows Riedel shears appropriate for that area.

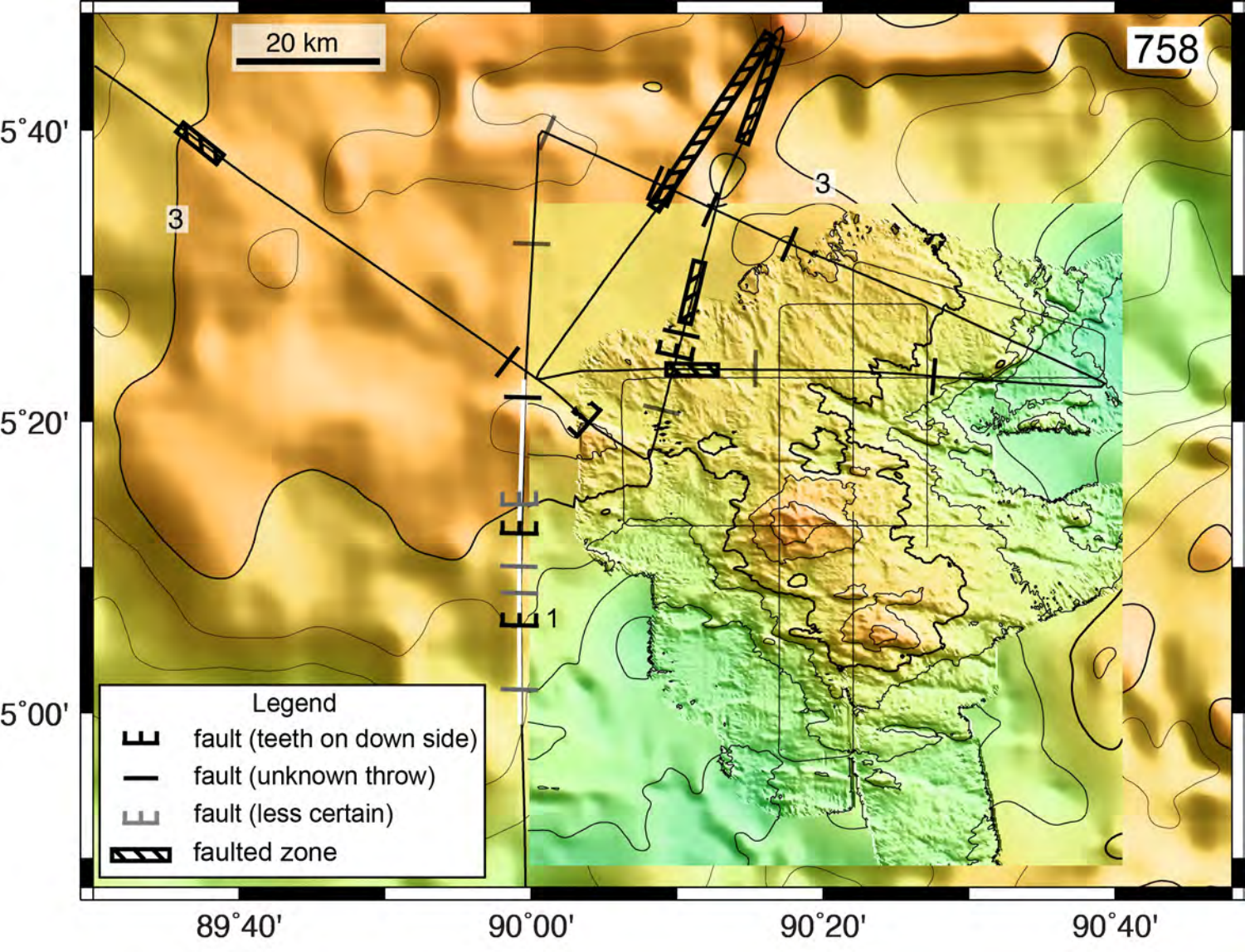
920







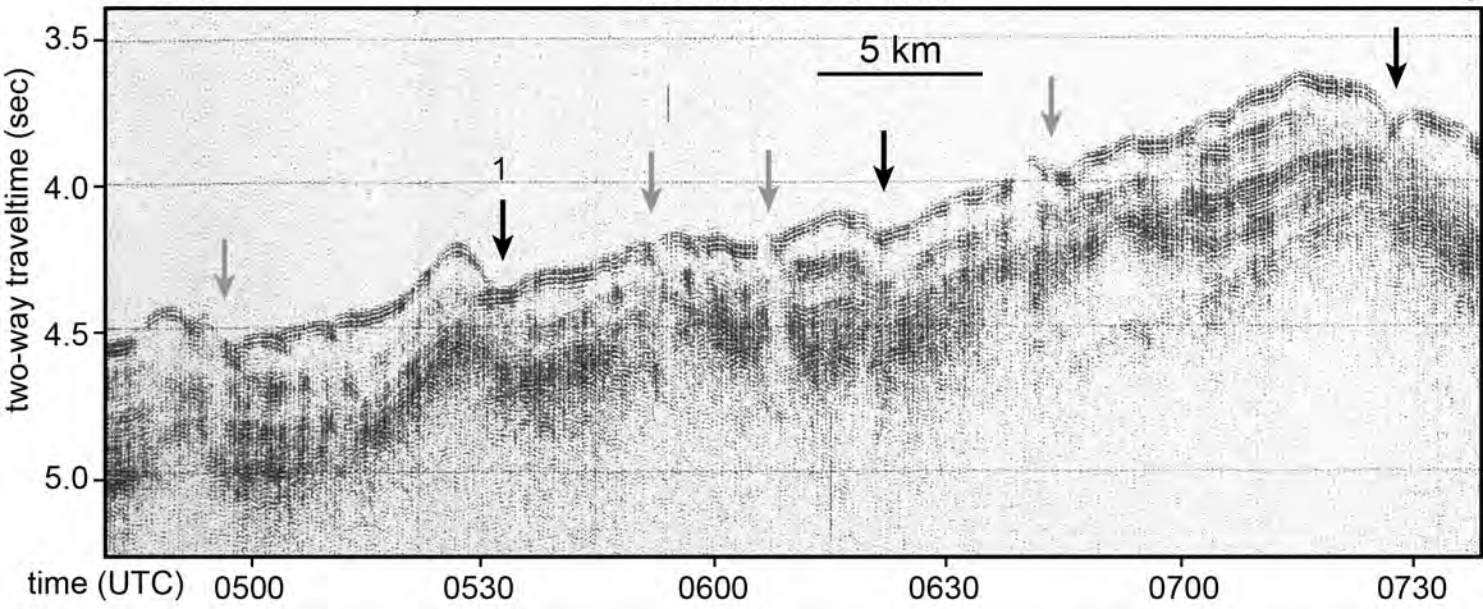


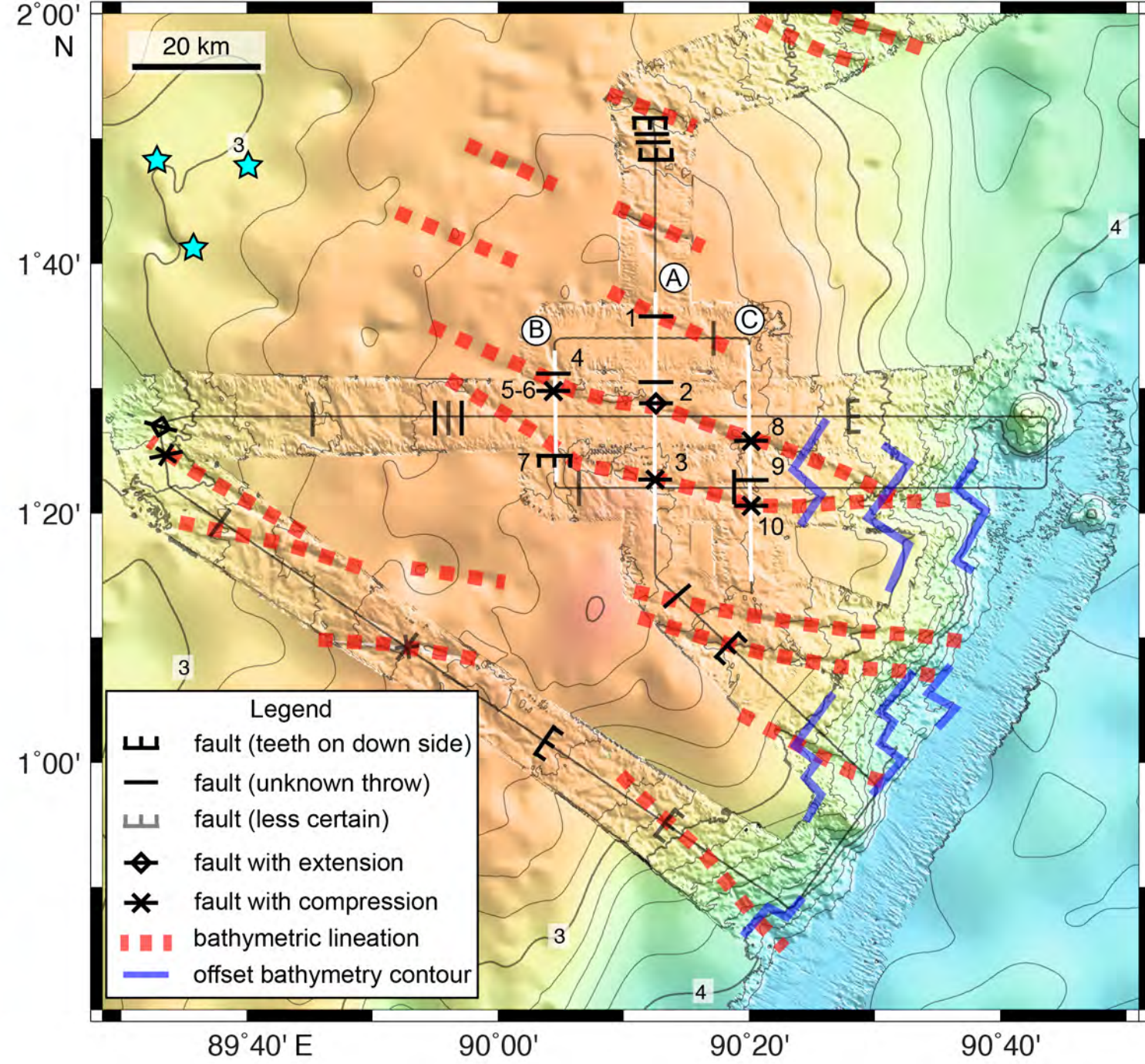
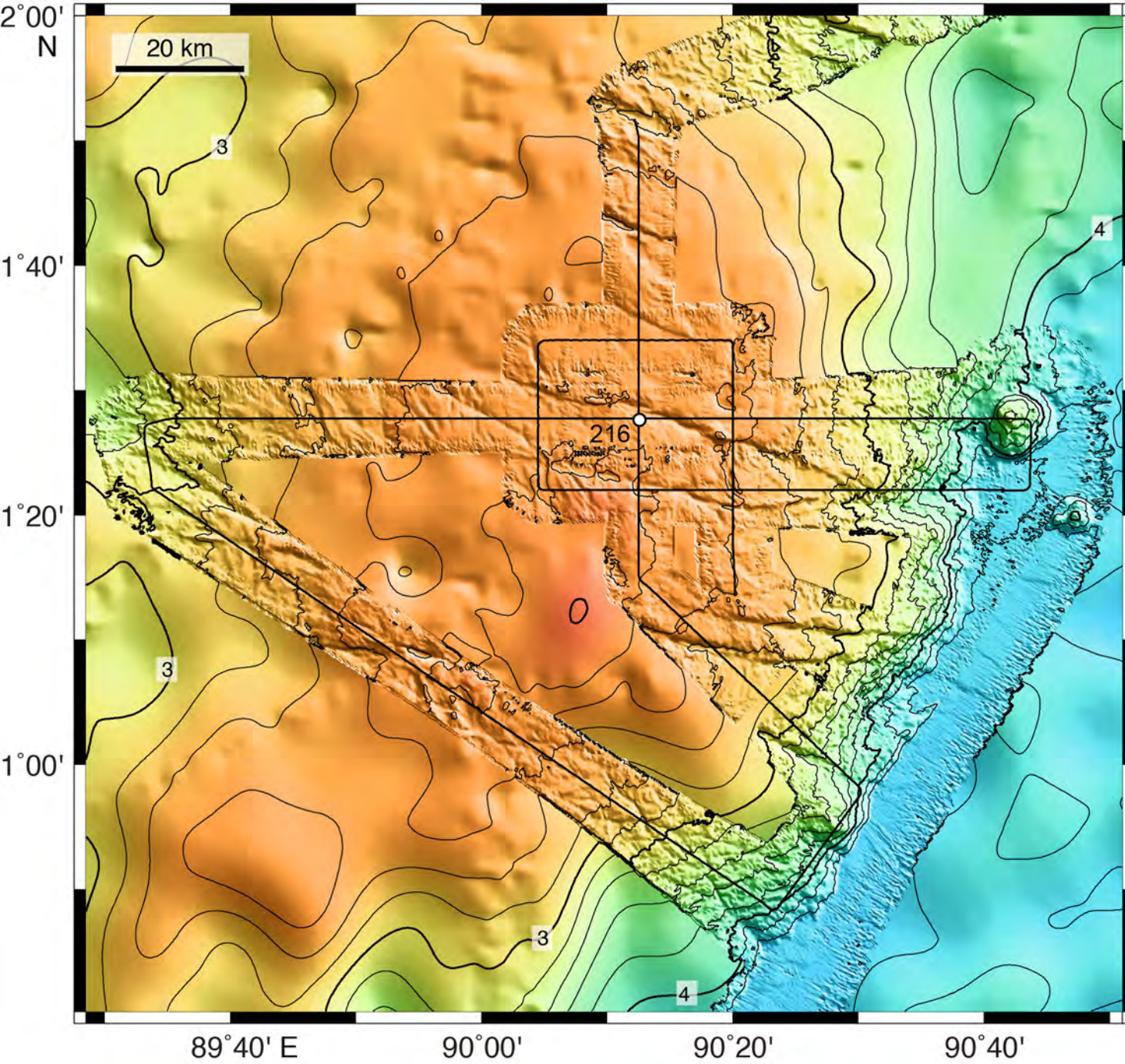


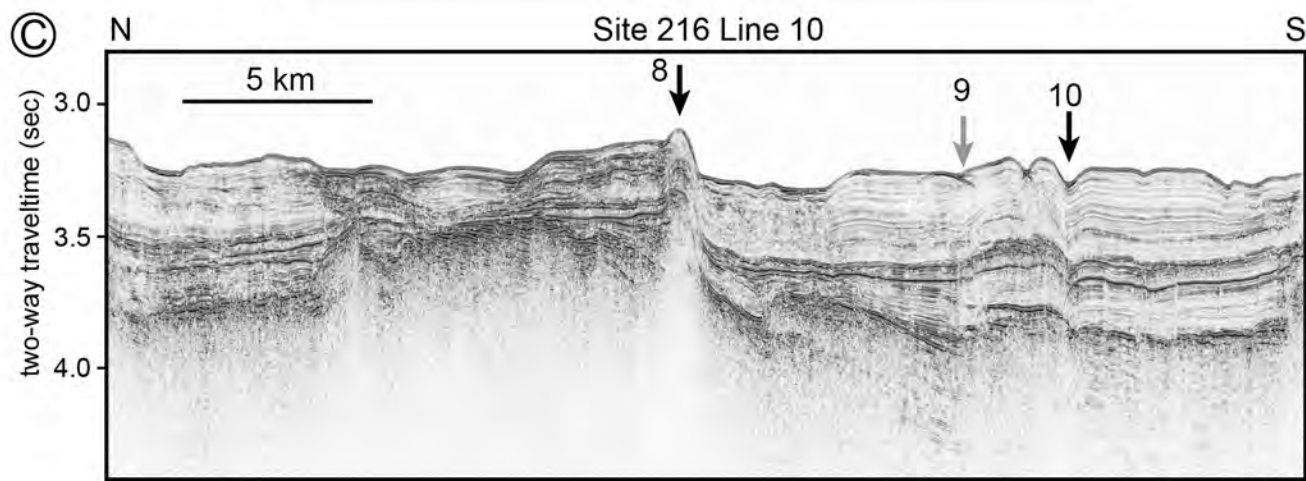
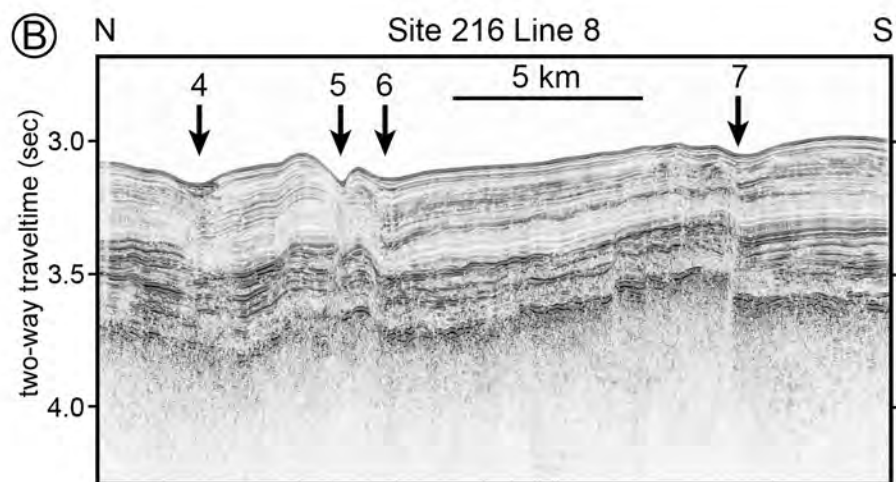
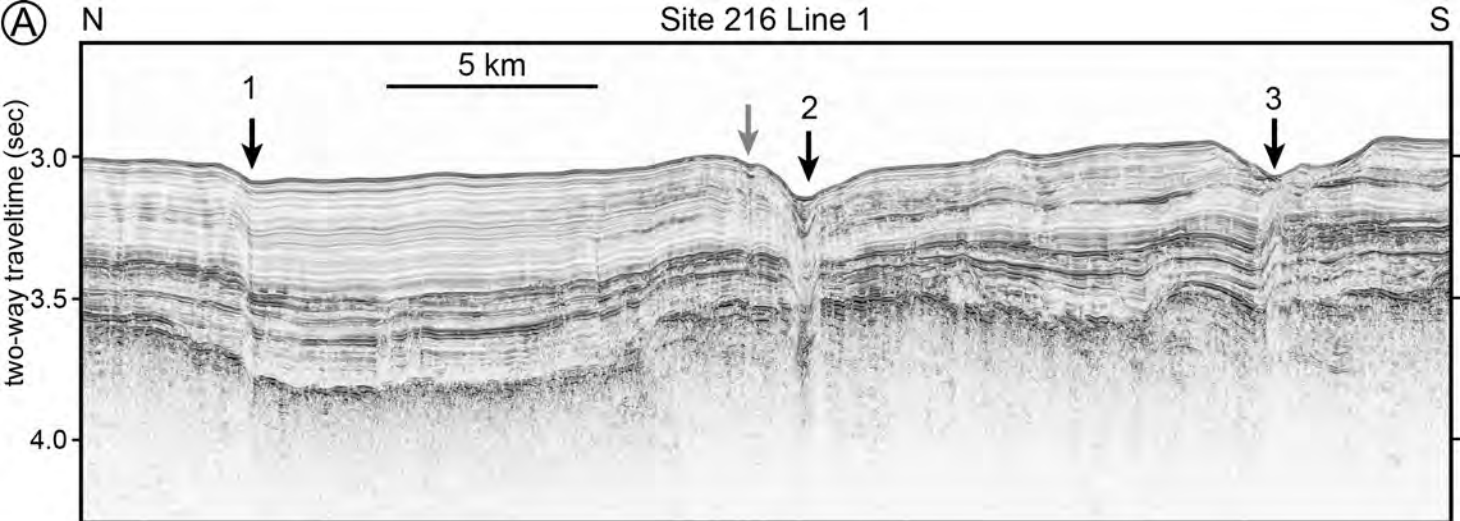
N Line 1

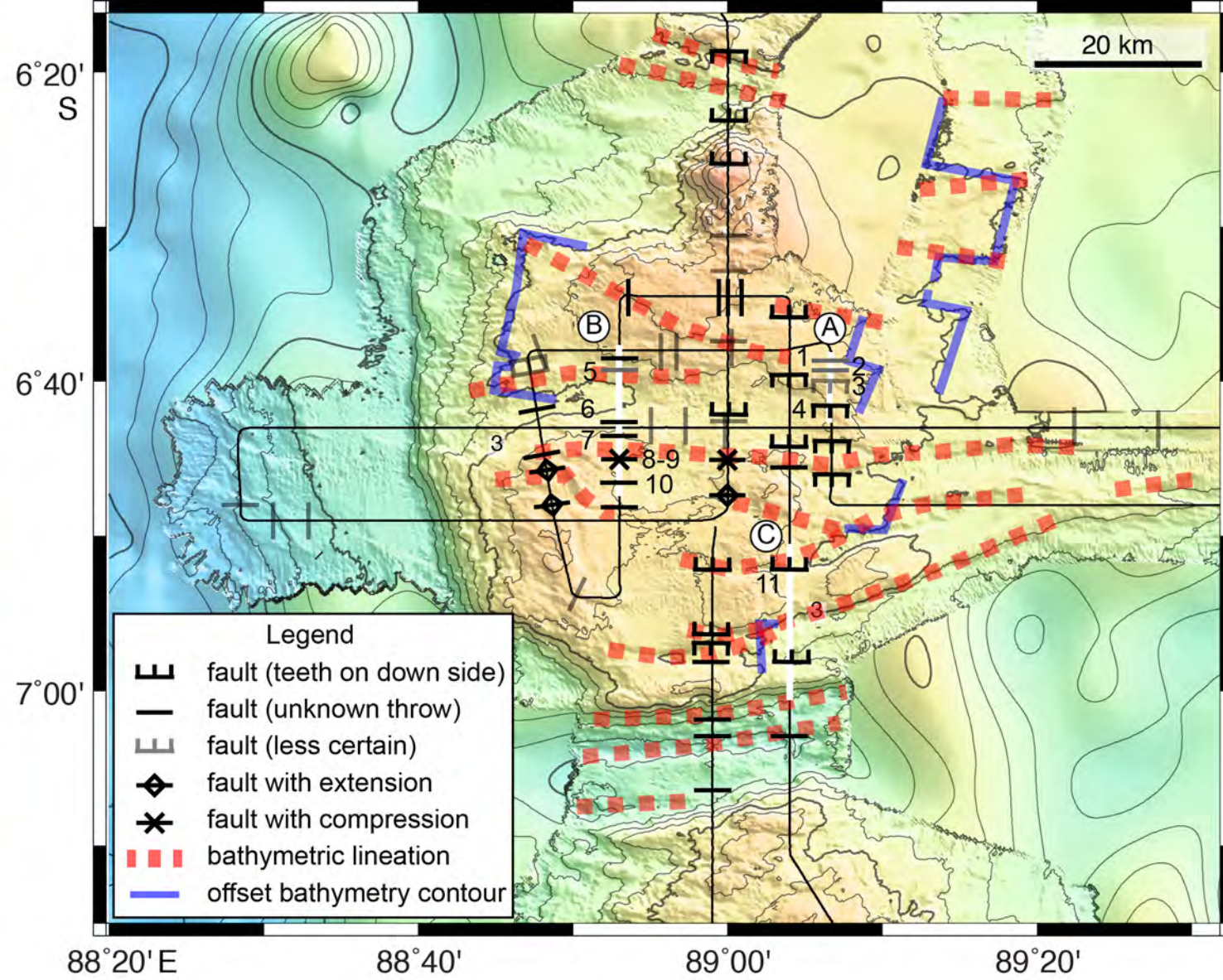
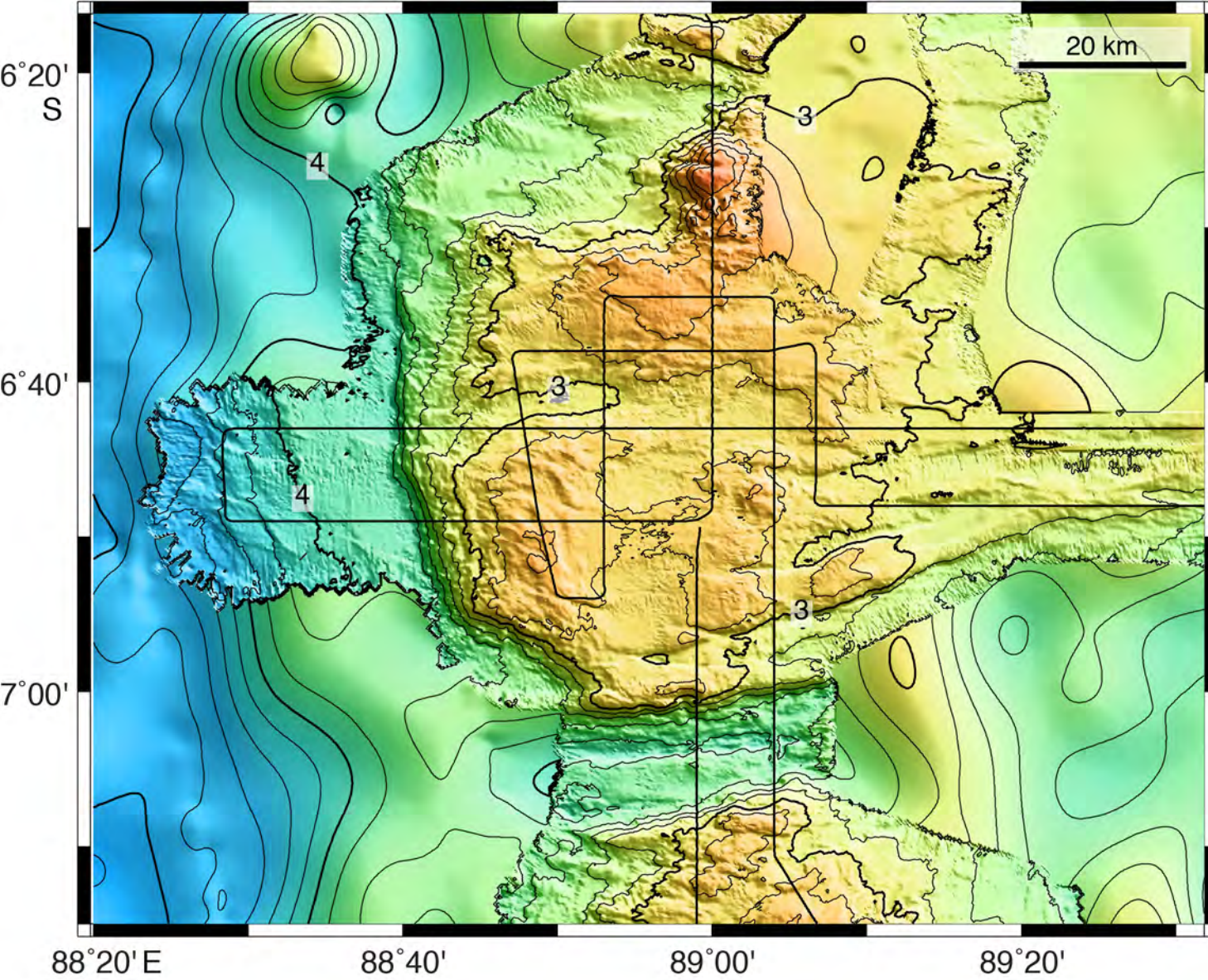
RC2705 25 June 1986

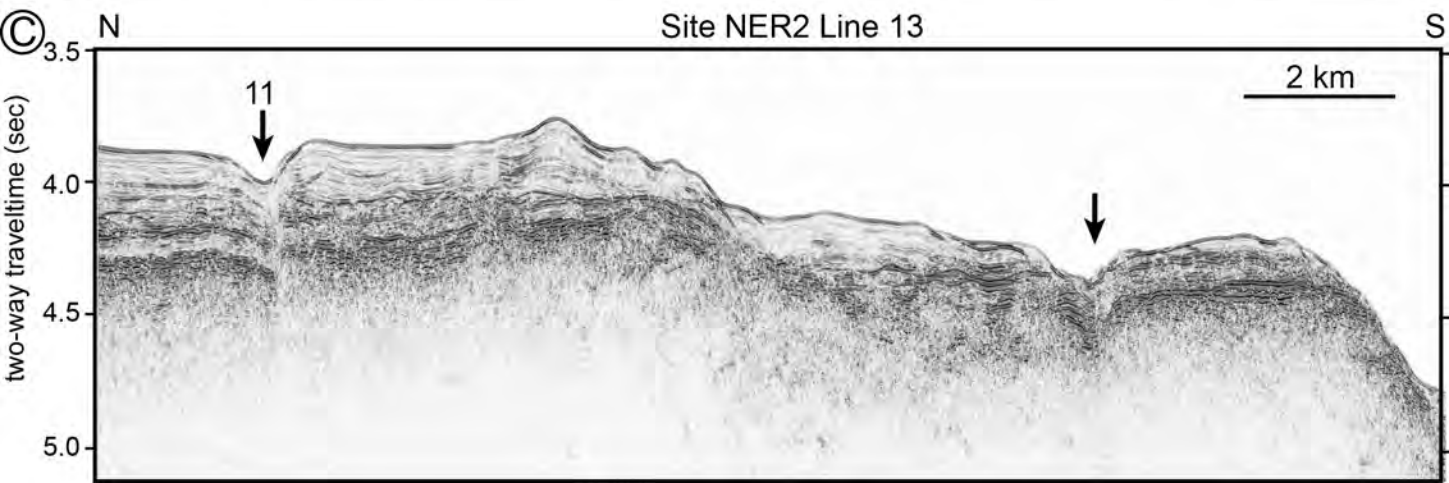
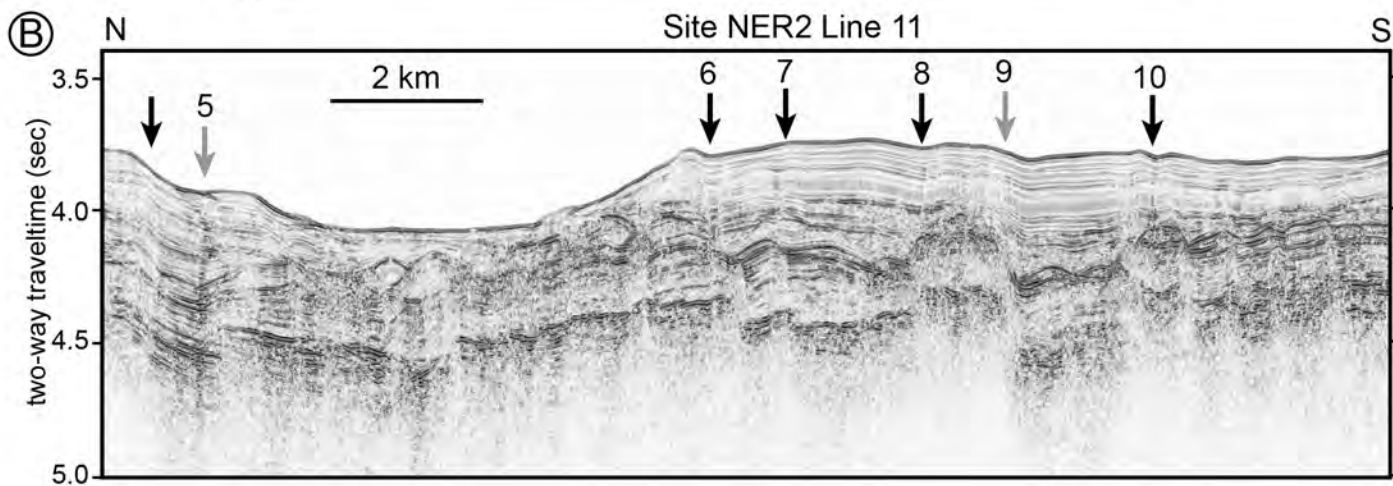
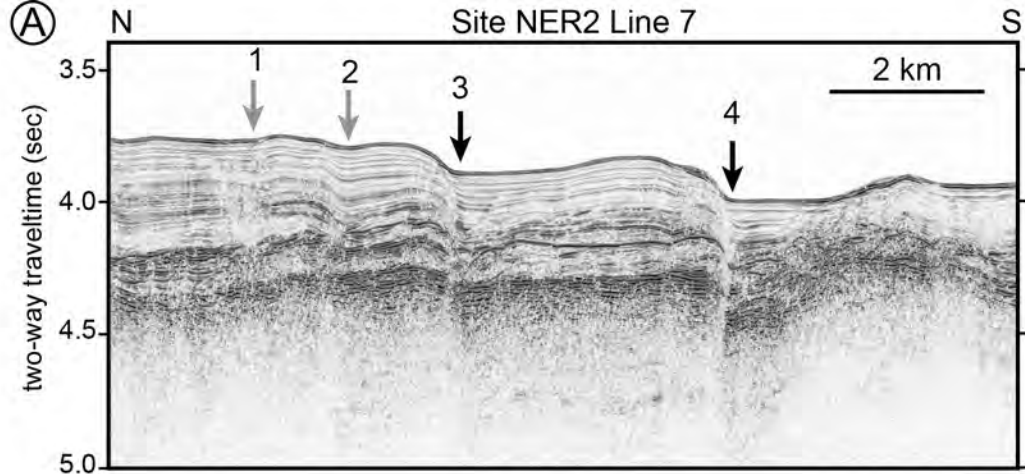
S

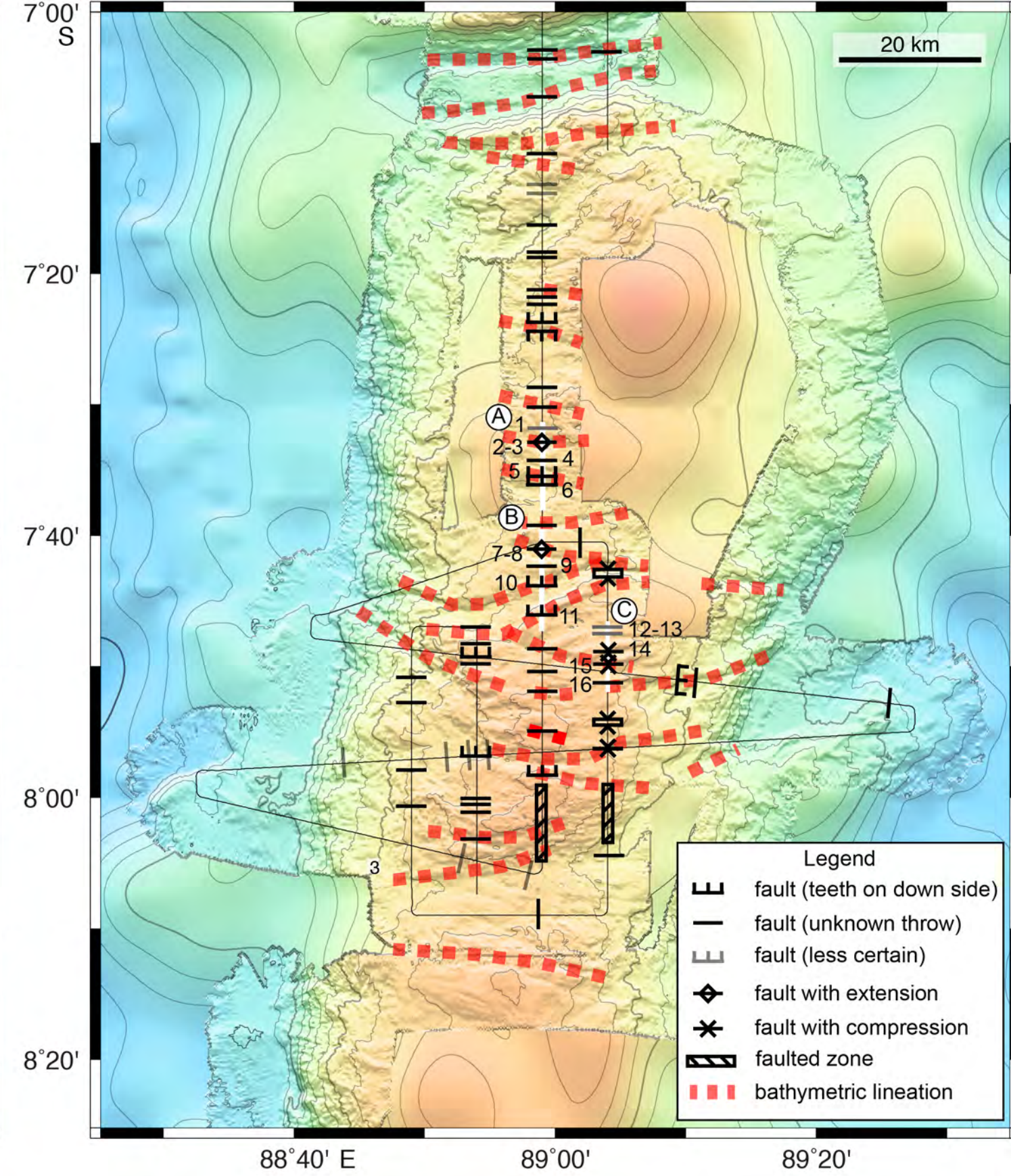
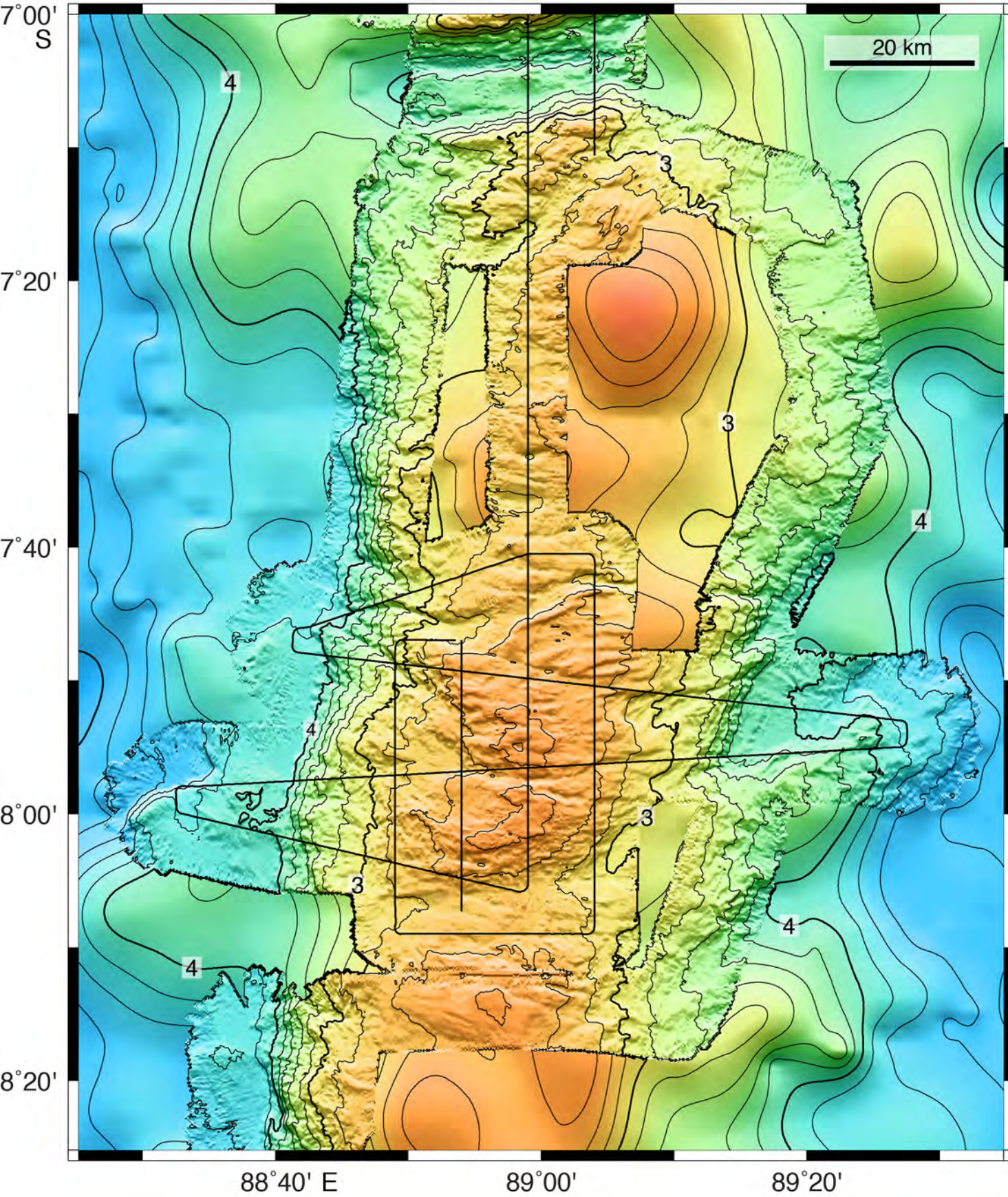


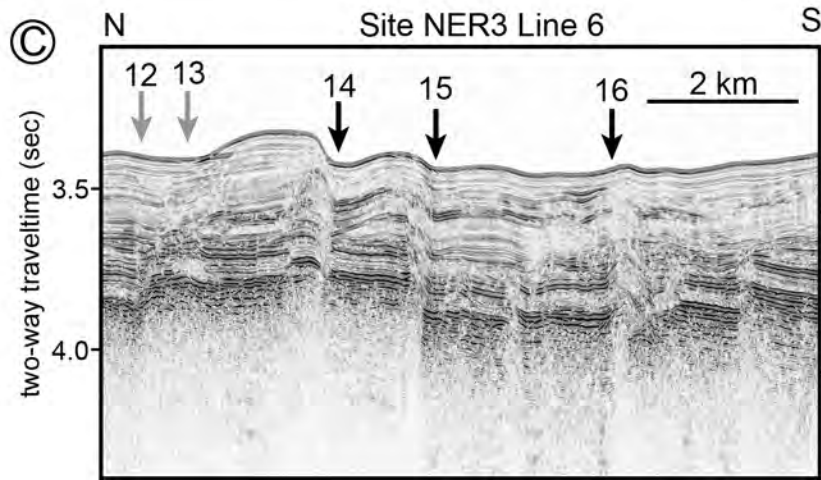
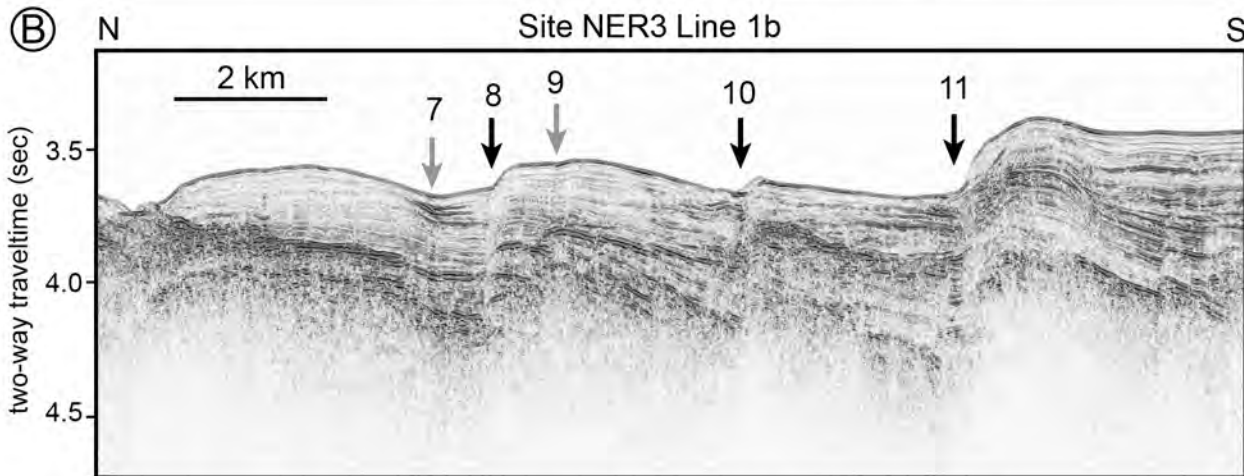
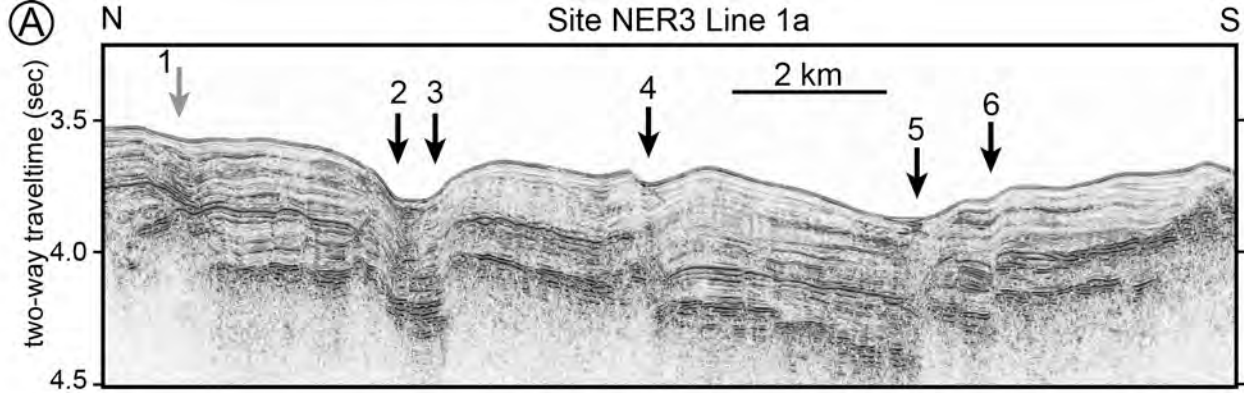


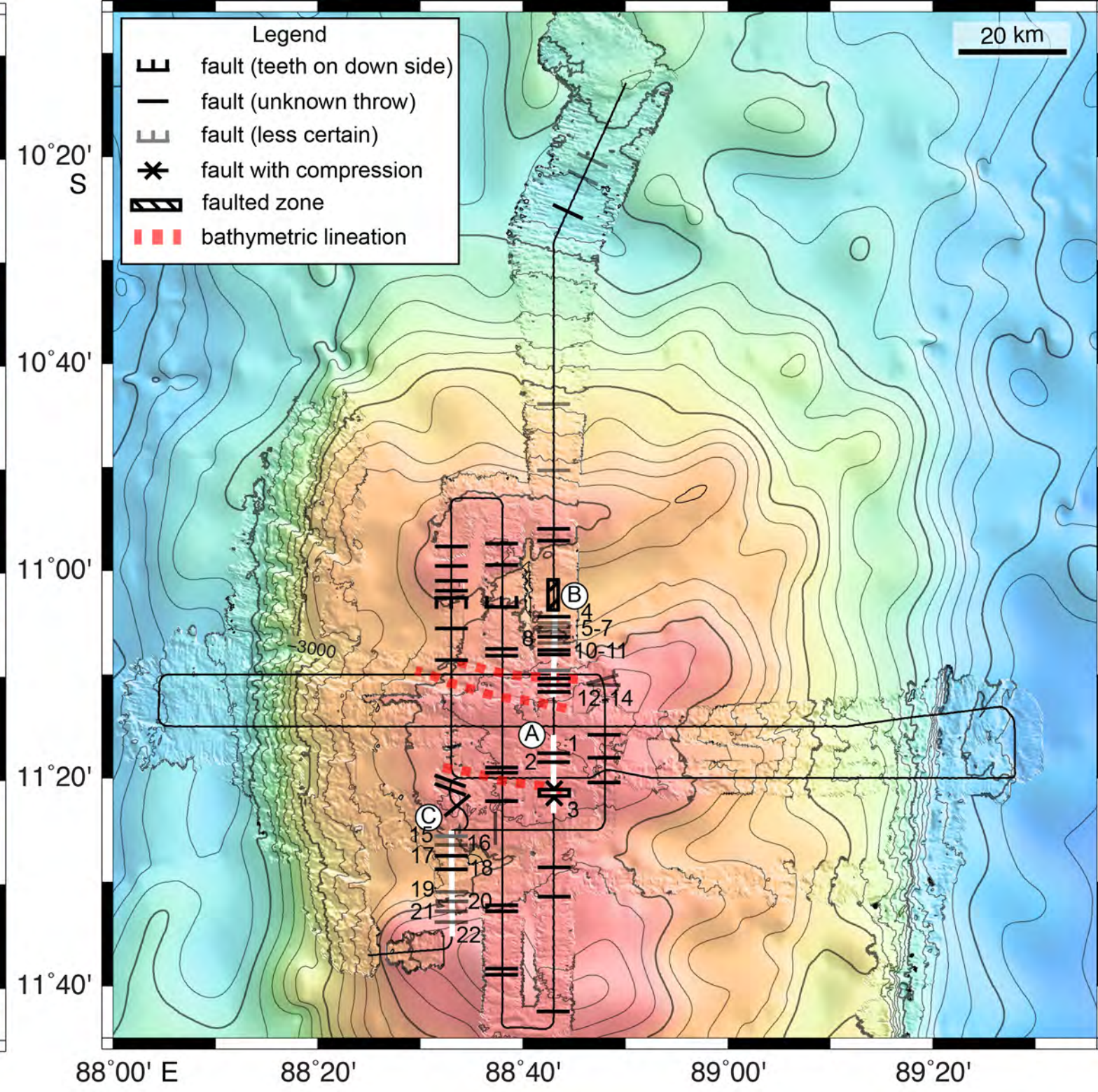
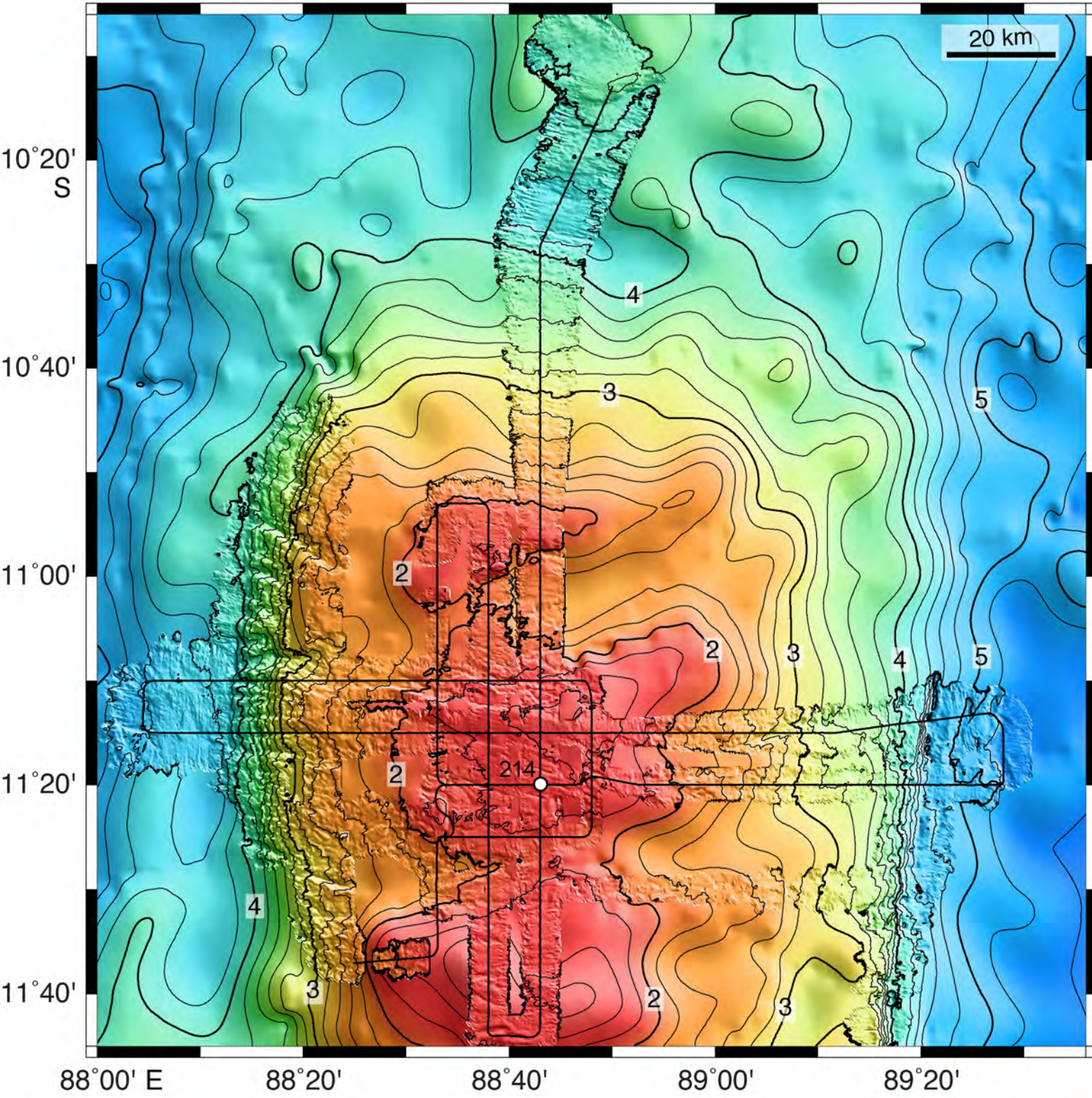


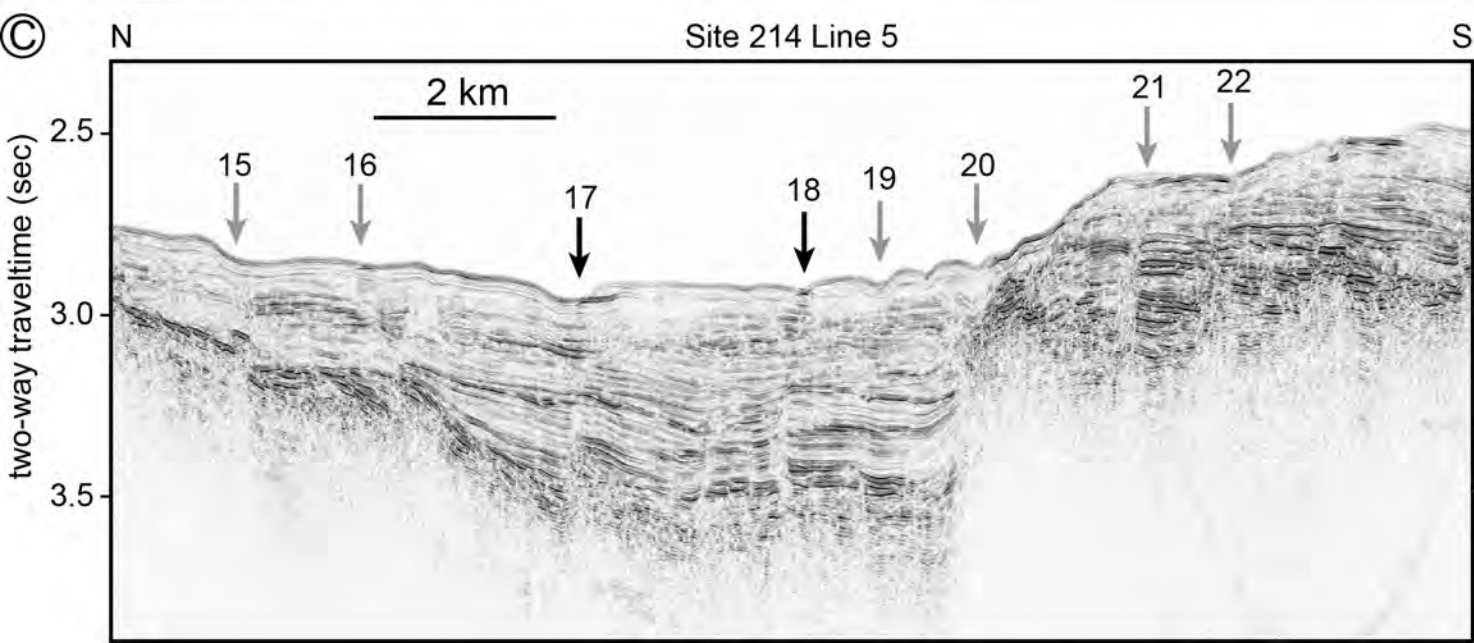
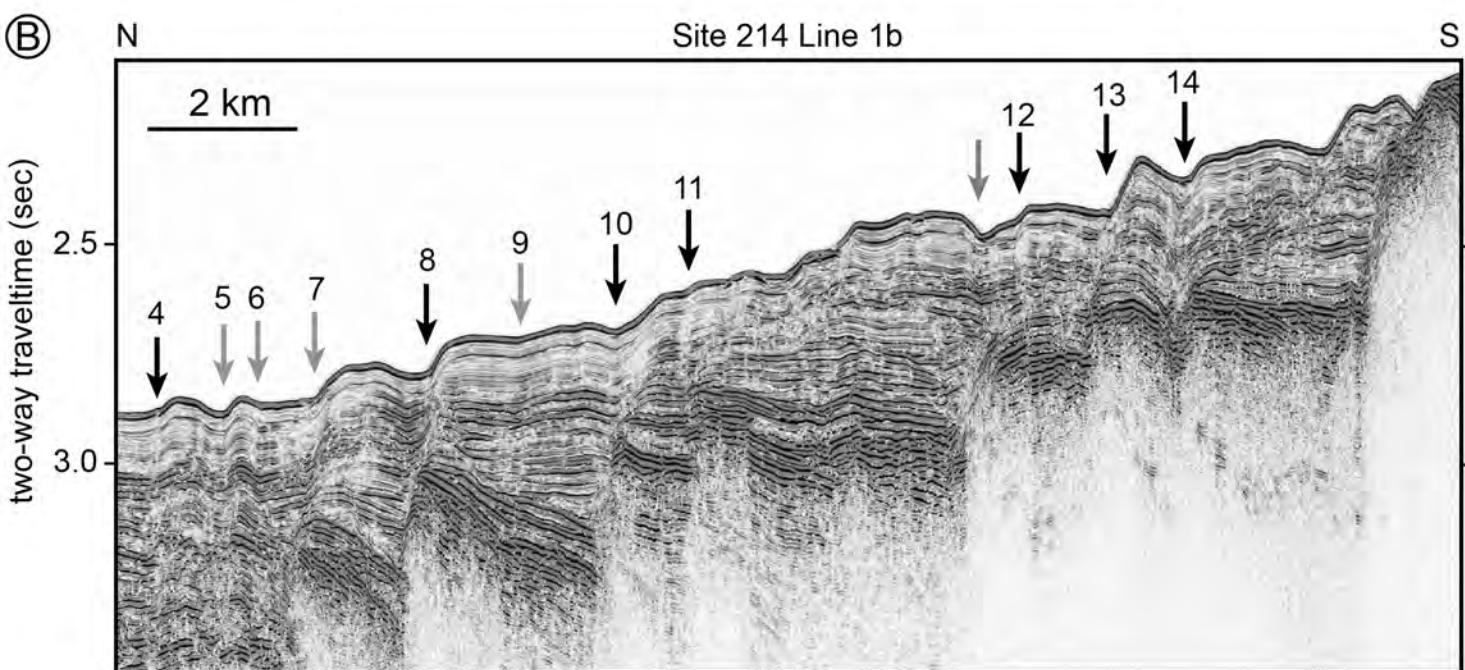
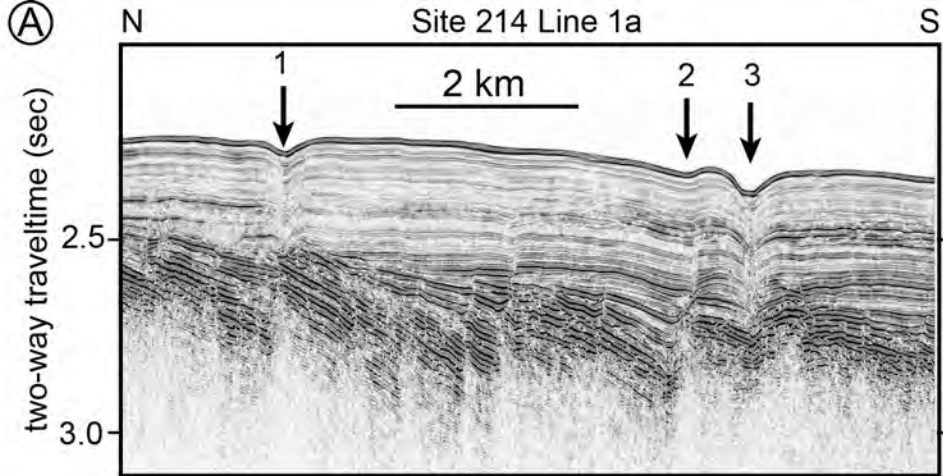


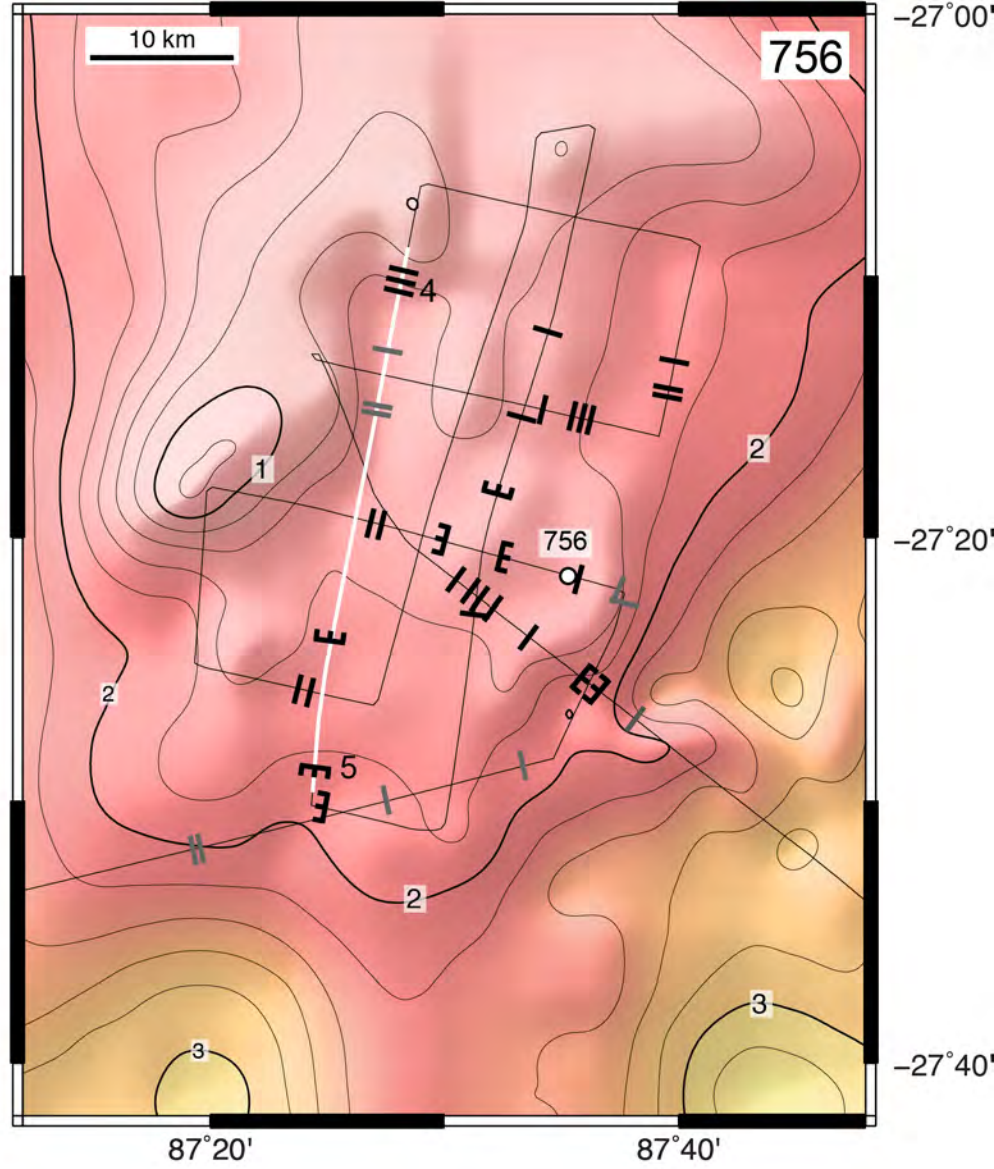
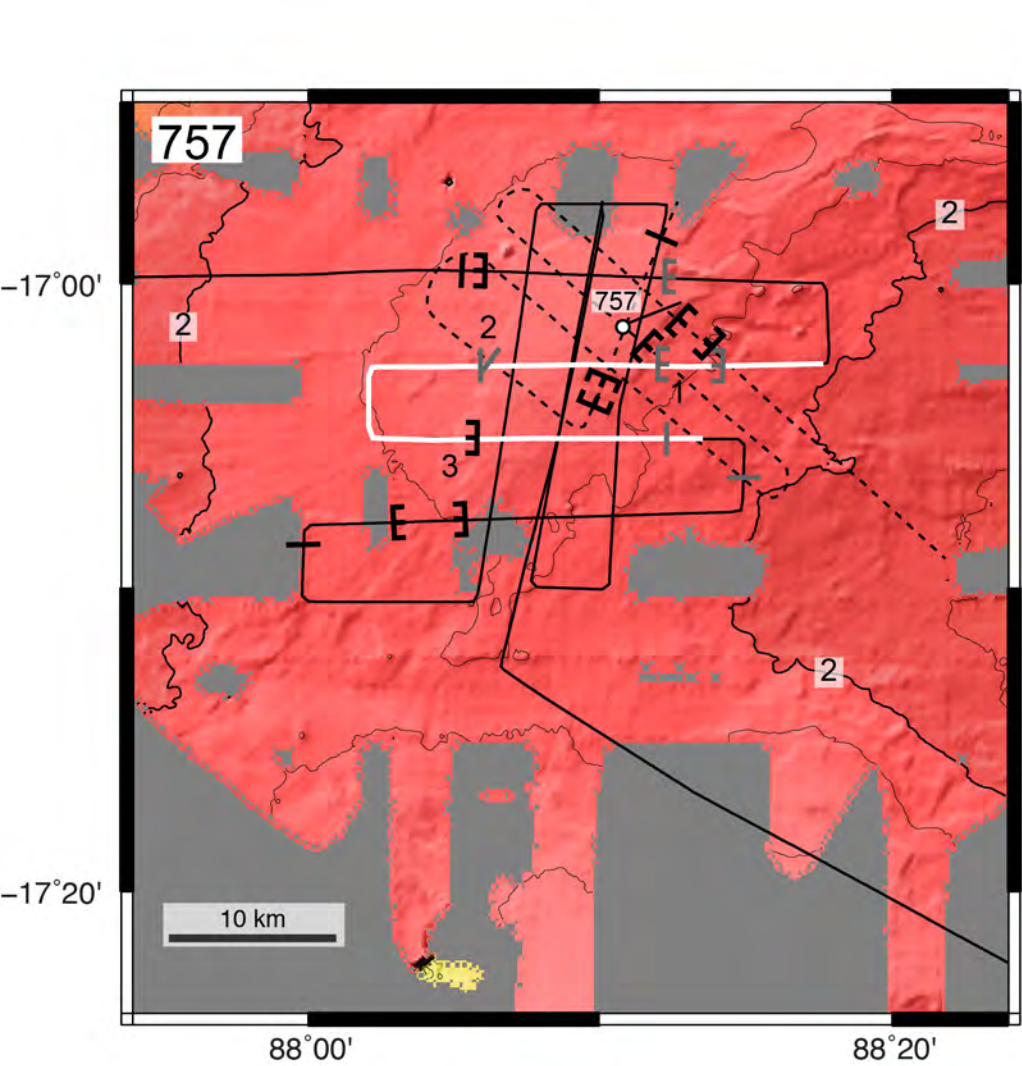




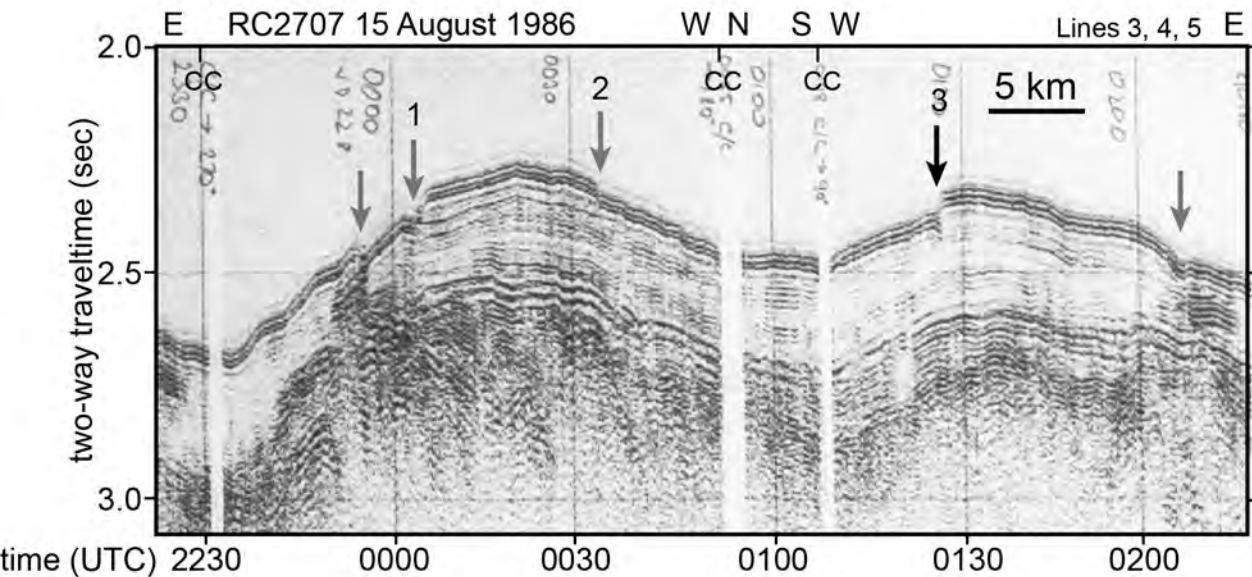








Site 757



Site 756

